

# $W^\pm Z$ production at the LHC: fiducial cross sections and distributions in NNLO QCD

Massimiliano Grazzini,<sup>a</sup> Stefan Kallweit,<sup>b</sup> Dirk Rathlev<sup>a</sup> and Marius Wiesemann<sup>a,b</sup>

<sup>a</sup>Physik-Institut, Universität Zürich,  
CH-8057 Zürich, Switzerland

<sup>b</sup>TH Division, Physics Department, CERN,  
CH-1211 Geneva 23, Switzerland

E-mail: [grazzini@physik.uzh.ch](mailto:grazzini@physik.uzh.ch), [stefan.kallweit@cern.ch](mailto:stefan.kallweit@cern.ch),  
[rathlev@physik.uzh.ch](mailto:rathlev@physik.uzh.ch), [marius.wiesemann@cern.ch](mailto:marius.wiesemann@cern.ch)

**ABSTRACT:** We report on the first fully differential calculation for  $W^\pm Z$  production in hadron collisions up to next-to-next-to-leading order (NNLO) in QCD perturbation theory. Leptonic decays of the  $W$  and  $Z$  bosons are consistently taken into account, i.e. we include all resonant and non-resonant diagrams that contribute to the process  $pp \rightarrow \ell'^\pm \nu_{\ell'} \ell^\pm \ell^\mp + X$  both in the same-flavour ( $\ell' = \ell$ ) and the different-flavour ( $\ell' \neq \ell$ ) channel. Fiducial cross sections and distributions are presented in the presence of standard selection cuts applied in the experimental  $W^\pm Z$  analyses by ATLAS and CMS at centre-of-mass energies of 8 and 13 TeV. As previously shown for the inclusive cross section, NNLO corrections increase the NNLO result by about 10%, thereby leading to an improved agreement with experimental data. The importance of NNLO accurate predictions is also shown in the case of new-physics scenarios, where, especially in high- $p_T$  categories, their impact can reach  $\mathcal{O}(20\%)$ . The availability of differential NNLO predictions will play a crucial role in the rich physics programme that is based on precision studies of  $W^\pm Z$  signatures at the LHC.

**KEYWORDS:** NLO Computations, QCD Phenomenology

**ARXIV EPRINT:** [1703.09065](https://arxiv.org/abs/1703.09065)

---

## Contents

<b>1</b>	<b>Introduction</b>	<b>1</b>
<b>2</b>	<b>Description of the calculation</b>	<b>3</b>
2.1	Organization of the calculation in MATRIX	5
2.2	Stability of $q_T$ subtraction for $W^\pm Z$ production	6
<b>3</b>	<b>Results</b>	<b>7</b>
3.1	Fiducial cross sections	8
3.1.1	ATLAS 8 TeV	9
3.1.2	ATLAS 13 TeV	11
3.1.3	CMS 13 TeV	11
3.2	Distributions in the fiducial phase space	11
3.3	New-physics searches	19
<b>4</b>	<b>Summary</b>	<b>28</b>
<b>A</b>	<b>CMS cross sections at 8 TeV and 13 TeV</b>	<b>31</b>

---

## 1 Introduction

The production of a pair of vector bosons is among the most relevant physics processes at the Large Hadron Collider (LHC). Besides playing a central role in precision tests of the gauge structure of electroweak (EW) interactions and in studies of the mechanism of EW symmetry breaking, vector-boson pair production constitutes an irreducible background in most of the Higgs-boson measurements and in many searches for physics beyond the Standard Model (SM).

The production of  $W^\pm Z$  pairs, in particular, offers a valuable test of the triple gauge-boson couplings, and is an important SM background in many SUSY searches (see e.g. ref. [1]). The  $W^\pm Z$  cross section has been measured at the Tevatron [2, 3] and at the LHC for centre-of-mass energies of 7 TeV [4, 5], 8 TeV [5, 6] and 13 TeV [7, 8]. Thanks to the increasing reach in energy of LHC Run 2, more statistics — the above-cited 13 TeV results are only based on the early 2015 data — will make  $W^\pm Z$  measurements a powerful tool to extend the current bounds on the corresponding anomalous couplings. To this purpose, a good control over the SM predictions in the tails of some kinematic distributions is particularly important. As a SM background,  $W^\pm Z$  production is especially relevant in searches based on final states with three leptons and missing transverse energy, which feature a clean experimental signature, but miss a full reconstruction of the  $W$  boson. As a result, the irreducible  $W^\pm Z$  background is not easily extracted from data with a

simple side-band approach. For the above reasons, the availability of accurate theoretical predictions of the differential  $W^\pm Z$  cross section is necessary in order to ensure a high sensitivity to anomalous couplings and to control the SM background in searches based on the trilepton plus missing transverse energy signature.

Accurate theoretical predictions for the  $W^\pm Z$  cross section were obtained at NLO in perturbative QCD a long time ago [9]. Leptonic decays of the  $W$  and  $Z$  bosons were added only a few years later [10], while initially omitting spin correlations in the virtual matrix elements. The first complete off-shell NLO computations, including leptonic decays and spin correlations, were performed [11–13] after the relevant one-loop helicity amplitudes [14] became available. The corresponding computation of the off-shell  $W^\pm Z$ +jet cross section in NLO QCD was presented in ref. [15]. EW corrections to  $W^\pm Z$  production are known only in an on-shell approach [16, 17] so far. Recently, the first NNLO QCD accurate prediction of the inclusive  $W^\pm Z$  cross section became available in ref. [18]. Due to the difference of the  $W$ - and  $Z$ -boson masses, this computation already used the off-shell two-loop helicity amplitudes of ref. [19] (another calculation of these amplitudes was described in ref. [20]), which allow for the computation of all vector-boson pair production processes, including leptonic decays, spin correlations and off-shell effects.

$W^\pm Z$  production is the only remaining di-boson process for which a fully exclusive NNLO calculation was not available so far. In this paper, we finally fill this gap by presenting, for the first time, NNLO-accurate fully differential predictions for the  $W^\pm Z$  cross section. More precisely, our off-shell calculation includes the leptonic decays of the vector bosons by considering the full process that leads to three leptons and one neutrino ( $\ell\ell\ell\nu$ ),  $pp \rightarrow \ell'^\pm \nu_{\ell'} \ell^+ \ell^- + X$ , in both the same-flavour ( $\ell' = \ell$ ) and the different-flavour ( $\ell' \neq \ell$ ) channel. Thereby, we take into account all non-resonant, single-resonant and double-resonant components, including intermediate  $W^\pm \gamma^*$  contributions and all interference effects as well as spin correlations and off-shell effects, consistently in the complex-mass scheme [21].

Our calculation is performed in the MATRIX<sup>1</sup> framework, which applies the  $q_T$ -subtraction [22] and -resummation [23] formalisms in their process-independent implementation within the Monte Carlo program MUNICH.<sup>2</sup> MUNICH facilitates the fully automated computation of NLO corrections to any SM process by using the Catani-Seymour dipole subtraction method [24, 25], an efficient phase-space integration, as well as an interface to the one-loop generator OPENLOOPS [26] to obtain all required (spin- and colour-correlated) tree-level and one-loop amplitudes. For the numerical stability in the tensor reductions of the one-loop amplitudes, OPENLOOPS relies on the COLLIER library [27, 28]. Our implementation of  $q_T$  subtraction and resummation<sup>3</sup> for the production of colourless final states

<sup>1</sup>MATRIX is the abbreviation of “MUNICH Automates qT subtraction and Resummation to Integrate X-sections”, by M. Grazzini, S. Kallweit, D. Rathlev, M. Wiesemann. In preparation.

<sup>2</sup>MUNICH is the abbreviation of “Multi-channel Integrator at Swiss (CH) precision” — an automated parton-level NLO generator by S. Kallweit. In preparation.

<sup>3</sup>The first application of the transverse-momentum resummation framework implemented in MATRIX at NNLL+NNLO to on-shell  $W^+W^-$  and  $ZZ$  production was presented in ref. [29] (see also ref. [30] for more details).

is fully general, and it is based on the universality of the hard-collinear coefficients [31] appearing in the transverse-momentum resummation formalism. These coefficients were explicitly computed for quark-initiated processes in refs. [32–34]. For the two-loop helicity amplitudes we use the results of ref. [19], and of ref. [35] for Drell-Yan like topologies. Their implementation in MATRIX is applicable to any  $\ell\ell\ell\nu$  final state. This widely automated framework has already been used, in combination with the two-loop scattering amplitudes of refs. [19, 36], for the calculations of  $Z\gamma$  [37, 38],  $ZZ$  [39, 40],  $W^+W^-$  [41, 42],  $W^\pm\gamma$  [38] and  $W^\pm Z$  [18] production at NNLO QCD as well as in the resummed computations of the  $ZZ$  and  $W^+W^-$  transverse-momentum spectra [29] at NNLL+NNLO.

NNLO corrections to the  $W^\pm Z$  process have been shown to be sizeable already in the case of the total inclusive cross section [18]. This is explained by the existence of an approximate radiation zero [43] at LO, which is broken only by real corrections starting at NLO. In this paper we will show that NNLO corrections to  $W^\pm Z$  production are equally relevant to provide reliable QCD predictions for fiducial cross sections and distributions, and to obtain agreement with the LHC data. At the same time, the inclusion of NNLO corrections will be shown to be essential to obtain a good control of SM backgrounds in SUSY searches based on the trilepton + missing energy signature [44].

The manuscript is organized as follows. In section 2 we give details on the technical implementation of our computation, including a brief introduction of the MATRIX framework (section 2.1) and a discussion of the stability of the  $W^\pm Z$  cross section at (N)NLO based on  $q_T$  subtraction (section 2.2). Section 3 gives an extensive collection of numerical results for  $pp \rightarrow \ell^{(\prime)\pm}\nu_{\ell^{(\prime)}}\ell^+\ell^- + X$  we present cross sections (section 3.1) and distributions (section 3.2) in the fiducial volume for  $W^\pm Z$  measurements, including their comparison to experimental data, where available, and with cuts corresponding to new-physics searches (section 3.3). The main results are summarized in section 4.

## 2 Description of the calculation

We study the process

$$pp \rightarrow \ell'^{\pm}\nu_{\ell'}\ell^+\ell^- + X, \quad \ell, \ell' \in \{e, \mu\}, \quad (2.1)$$

including all Feynman diagrams that contribute to the production of three charged leptons — one opposite-sign, same-flavour (OSSF) lepton pair, and another charged lepton of either the same ( $\ell' = \ell$ ) or a different ( $\ell' \neq \ell$ ) flavour, later referred to as same-flavour (SF) and different-flavour (DF) channel — and one corresponding neutrino.

Our calculation is performed in the complex-mass scheme [21], and besides resonances, it includes also contributions from off-shell EW bosons and all relevant interferences; no resonance approximation is applied. Our implementation can deal with any combination of leptonic flavours,  $\ell, \ell' \in \{e, \mu, \tau\}$ . For the sake of brevity, we will often denote this process as  $W^\pm Z$  production though.

The  $\ell\ell\ell\nu$  final states are generated, as shown in figure 1 for the  $u\bar{d} \rightarrow \ell'^+\nu_{\ell'}\ell^-\ell^+$  process at LO,

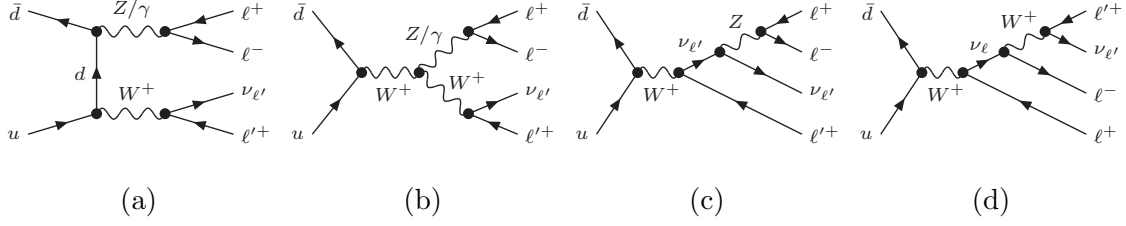


**Figure 1.** Sample of Born diagrams contributing to  $W^+Z$  production both in the different-flavour channel ( $\ell \neq \ell'$ ) and in the same-flavour channel ( $\ell = \ell'$ ). The analogous diagrams for  $W^-Z$  production are achieved by charge conjugation.

- (a) via resonant  $t$ -channel  $W^\pm Z$  production with subsequent  $W^\pm \rightarrow \ell'^\pm \nu_{\ell'}$  and  $Z \rightarrow \ell^- \ell^+$  decays, where the intermediate  $Z$  boson can be replaced by an off-shell photon  $\gamma^*$ ;
- (b) via  $s$ -channel production in  $W^\pm \rightarrow W^\pm Z / W^\pm \gamma^*$  topologies through a triple-gauge-boson vertex  $WWZ$  or  $WW\gamma$  with subsequent  $W^\pm \rightarrow \ell'^\pm \nu_{\ell'}$  and  $Z/\gamma^* \rightarrow \ell^- \ell^+$  decays;
- (c) via  $W^{\pm(*)}$  production with a subsequent decay  $W^{\pm(*)} \rightarrow \ell'^\pm \nu_{\ell'} Z^{(*)} / \gamma^* \rightarrow \ell'^\pm \nu_{\ell'} \ell^- \ell^+$ ;
- (d) via  $W^{\pm(*)}$  production with a subsequent decay  $W^{\pm(*)} \rightarrow \ell^- \ell^+ W^{\pm(*)} \rightarrow \ell'^\pm \nu_{\ell'} \ell^- \ell^+$ .

In the SF channel, each diagram has to be supplemented with the analogous diagram obtained by exchanging the momenta of the identical charged leptons, but the generic resonance structure is not modified as compared to the DF channel. Note that in both SF and DF channels the appearance of infrared (IR) divergent  $\gamma^* \rightarrow \ell^- \ell^+$  splittings prevents a fully inclusive phase-space integration for massless leptons. In the DF channel, the usual experimental requirement of a mass window around the  $Z$ -boson mass for the OSSF lepton pair is already sufficient to avoid such divergences and render the cross section finite, while in the SF channel a lepton separation must be applied on both possible combinations of OSSF lepton pairs.

The NNLO computation requires the following scattering amplitudes at  $\mathcal{O}(\alpha_S^2)$ :

- tree amplitudes for  $q\bar{q}' \rightarrow \ell'^\pm \nu_{\ell'} \ell^- \ell^+ gg$ ,  $q\bar{q}' \rightarrow \ell'^\pm \nu_{\ell'} \ell^- \ell^+ q''\bar{q}''$ , and crossing-related processes;
- one-loop amplitudes for  $q\bar{q}' \rightarrow \ell'^\pm \nu_{\ell'} \ell^- \ell^+ g$ , and crossing-related processes;
- squared one-loop and two-loop amplitudes for  $q\bar{q}' \rightarrow \ell'^\pm \nu_{\ell'} \ell^- \ell^+$ .

The  $q\bar{q}'$  pair is of type  $u\bar{d}$  and  $d\bar{u}$  for  $W^+Z$  and  $W^-Z$  production, respectively, and  $q'' = q$  or  $q'' = q'$  are explicitly allowed. Note that there is no loop-induced  $gg$  channel in  $W^\pm Z$  production due to the electric charge of the final state.

All required tree-level and one-loop amplitudes are obtained from the OPENLOOPS generator [26, 45], which implements a fast numerical recursion for the calculation of NLO scattering amplitudes within the SM. For the numerically stable evaluation of tensor integrals we employ the COLLIER library [27, 28, 46], which is based on the Denner-Dittmaier

reduction techniques [47, 48] and the scalar integrals of ref. [49]. To guarantee numerical stability in exceptional phase-space regions — more precisely for phase-space points where the two independent tensor-reduction implementations of COLLIER disagree by more than a certain threshold — OPENLOOPS provides a rescue system based on the quadruple-precision implementation of CUTTOOLS [50], which applies scalar integrals from ONELOOP [51].

For the two-loop helicity amplitudes we rely on a public C++ library [52] that implements the results of ref. [19], and for the numerical evaluation of the relevant multiple polylogarithms we use the implementation [53] in the GINAC [54] library. The contribution of the massive-quark loops is neglected in the two-loop amplitudes, but accounted for everywhere else.

## 2.1 Organization of the calculation in MATRIX

The widely automated framework MATRIX is used for our NNLO calculation of the  $W^\pm Z$  cross section. MATRIX entails a fully automated implementation of the  $q_T$ -subtraction formalism to compute NNLO corrections, and is thus applicable to any production process of an arbitrary set of colourless final-state particles in hadronic collisions, as long as the respective two-loop virtual amplitudes of the Born-level process are known. On the same basis MATRIX automates also the small- $q_T$  resummation of logarithmically enhanced terms at NNLL accuracy (see ref. [29], and ref. [30] for more details).

The core of the MATRIX framework is the Monte Carlo program MUNICH, which includes a fully automated implementation of the Catani-Seymour dipole-subtraction method for massless [24, 25] and massive [55] partons, an efficient phase-space integration, as well as an interface to the one-loop generator OPENLOOPS [26, 45] to obtain all required (spin- and colour-correlated) tree-level and one-loop amplitudes. The extension of MUNICH and OPENLOOPS to deal with EW corrections [56, 57] allows for the fully automated computation of EW and QCD corrections to arbitrary SM processes at NLO accuracy.

Through an extension of MUNICH by a generic implementation of the  $q_T$ -subtraction and -resummation techniques, MATRIX achieves NNLL+NNLO accuracy in QCD for the production of colourless final states at a level of automation that is limited only by the process dependence of the two-loop amplitudes that enter the hard-collinear coefficient  $\mathcal{H}_{\text{NNLO}}^F$ . Any other process-dependent constituents of the calculation are formally (N)LO quantities and can thus be automatically computed by MUNICH+OPENLOOPS.

In order to give some technical details on its practical implementation, we recall the master formula for  $q_T$ -subtraction for the calculation of the  $pp \rightarrow F + X$  cross section at (N)NLO accuracy:

$$d\sigma_{(\text{N})\text{NLO}}^F = \mathcal{H}_{(\text{N})\text{NLO}}^F \otimes d\sigma_{\text{LO}}^F + \left[ d\sigma_{(\text{N})\text{LO}}^{F+\text{jet}} - d\sigma_{(\text{N})\text{NLO}}^{\text{CT}} \right]. \quad (2.2)$$

In eq. (2.2) the label  $F$  denotes an arbitrary combination of colourless particles and  $d\sigma_{(\text{N})\text{LO}}^{F+\text{jet}}$  is the (N)LO cross section for  $F + \text{jet}$  production. The explicit expression of the process-independent counterterm  $d\sigma_{(\text{N})\text{NLO}}^{\text{CT}}$  is provided in ref. [23]. The general structure of the hard-collinear coefficient  $\mathcal{H}_{\text{NLO}}^F$  is known from ref. [58], and that of  $\mathcal{H}_{\text{NNLO}}^F$  from ref. [31].

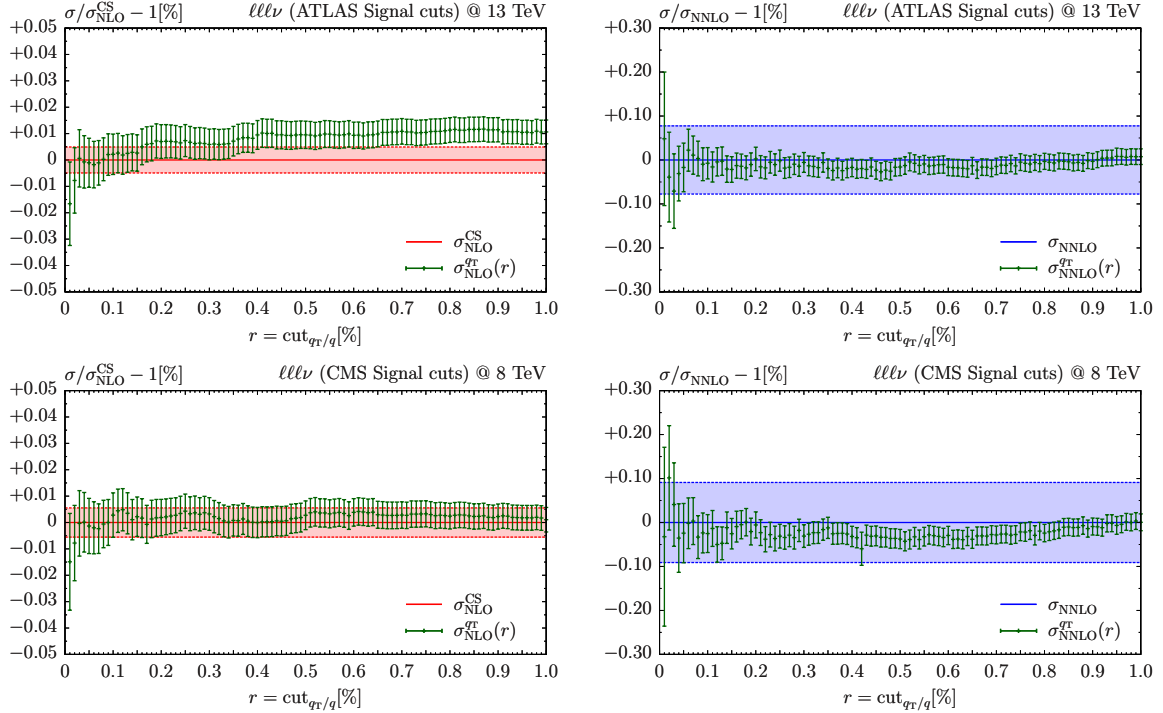


**Figure 2.** Dependence of the  $pp \rightarrow \ell'^{\pm} \nu_{\ell'} \ell^{-} \ell^{+} + X$  cross sections on the  $q_T$ -subtraction cut,  $r_{\text{cut}}$ , for both NLO (left plots) and NNLO (right plots) results in the ATLAS signal region at 13 TeV (upper plots) and in the CMS signal region at 8 TeV cuts (lower plots). NLO results are normalized to the  $r_{\text{cut}}$ -independent NLO cross section computed with Catani-Seymour subtraction, and the NNLO results are normalized to their values at  $r_{\text{cut}} \rightarrow 0$ , with a conservative extrapolation error indicated by the blue bands.

The latter exploits the explicit results for Higgs [59] and vector-boson [32] production. More details on the implementation of eq. (2.2) in MATRIX can be found in ref. [42].

The subtraction in the square brackets of eq. (2.2) is not local, but the cross section is formally finite in the limit  $q_T \rightarrow 0$ . In practice, a technical cut on  $q_T$  is introduced to render  $d\sigma_{(\text{N})\text{LO}}^{\text{F+jet}}$  and  $d\sigma_{(\text{N})\text{NLO}}^{\text{CT}}$  separately finite. In this respect, the  $q_T$ -subtraction method is very similar to a phase-space slicing method. It turns out that a cut,  $r_{\text{cut}}$ , on the dimensionless quantity  $r = q_T/M$ , where  $M$  denotes the invariant mass of F, is more convenient from a practical point of view. The absence of any residual logarithmic dependence on  $r_{\text{cut}}$  is a strong evidence of the correctness of the computation as any mismatch between the contributions would result in a divergence of the cross section when  $r_{\text{cut}} \rightarrow 0$ . The remaining power-suppressed contributions vanish in that limit, and can be controlled by monitoring the  $r_{\text{cut}}$  dependence of the cross section.

## 2.2 Stability of $q_T$ subtraction for $W^{\pm}Z$ production

In the following we investigate the stability of the  $q_T$ -subtraction approach for  $pp \rightarrow \ell'^{\pm} \nu_{\ell'} \ell^{-} \ell^{+} + X$ . To this end, in figure 2 we plot the NLO and NNLO cross sections as functions of the  $q_T$ -subtraction cut,  $r_{\text{cut}}$ , which acts on the dimensionless variable



$r = p_{T,\ell^\pm\nu_{\ell'}\ell^-\ell^+}/m_{\ell^\pm\nu_{\ell'}\ell^-\ell^+}$ . Sample validation plots are presented for two scenarios investigated in this paper, namely the ATLAS analysis at 13 TeV and the CMS analysis at 8 TeV (see section 3.1), summed over all leptonic channels contributing to the  $\ell\ell\ell\nu$  final state. All other scenarios considered in the paper lead essentially to the same conclusions.

At NLO the  $r_{\text{cut}}$ -independent cross section obtained with Catani-Seymour subtraction is used as a reference for the validation of the  $q_T$ -subtraction result. The comparison of the NLO cross sections in the left panels of figure 2 demonstrates that  $q_T$  subtraction agrees on the sub-permille level with the  $r_{\text{cut}}$ -independent result. This is true already at the moderate value of  $r_{\text{cut}} = 1\%$ .

At NNLO, where an  $r_{\text{cut}}$ -independent control result is not available, we observe no significant, i.e. beyond the numerical uncertainties,  $r_{\text{cut}}$  dependence below about  $r_{\text{cut}} = 1\%$ ; we thus use the finite- $r_{\text{cut}}$  results to extrapolate to  $r_{\text{cut}} = 0$ , taking into account the breakdown of predictivity for very low  $r_{\text{cut}}$  values, and conservatively estimate a numerical error due to the  $r_{\text{cut}}$  dependence of our results.<sup>4</sup> This procedure allows us to control all NNLO predictions for fiducial cross sections presented in section 3 to better than one per mille in terms of numerical uncertainties. An analogous bin-wise extrapolation procedure was also performed for all distributions under consideration in section 3, and no significant dependence on  $r_{\text{cut}}$  was found, thus confirming the robustness of our results also at the differential level.

### 3 Results

In this section we present our results on fiducial cross sections and distributions for  $W^\pm Z$  production in proton-proton collisions defined in eq. (2.1). We thus consider the inclusive production of three leptons and one neutrino including all possible flavour combinations, apart from channels involving  $\tau$  leptons. In particular, this involves the SF channels  $e^\pm e^+ e^-$  and  $\mu^\pm \mu^+ \mu^-$  as well as the DF channels  $\mu^\pm e^+ e^-$  and  $e^\pm \mu^+ \mu^-$ . Because of the availability of experimental results we consider LHC energies of 8 and 13 TeV and compare our predictions to the respective measurements by ATLAS and CMS. We finally study the impact of QCD radiative corrections when selection cuts designed for new physics searches are applied.

For the input of the weak parameters we apply the  $G_\mu$  scheme with complex  $W$ - and  $Z$ -boson masses to define the EW mixing angle as  $\cos\theta_W^2 = (m_W^2 - i\Gamma_W m_W)/(m_Z^2 - i\Gamma_Z m_Z)$ . We use the PDG [60] values  $G_F = 1.16639 \times 10^{-5} \text{ GeV}^{-2}$ ,  $m_W = 80.385 \text{ GeV}$ ,  $\Gamma_W = 2.0854 \text{ GeV}$ ,  $m_Z = 91.1876 \text{ GeV}$ ,  $\Gamma_Z = 2.4952 \text{ GeV}$ , and  $m_t = 173.2 \text{ GeV}$ . The CKM matrix is set to unity.<sup>5</sup>

We consider  $N_f = 5$  massless quark flavours, and we use the corresponding NNPDF3.0 [61] sets of parton distributions (PDFs) with  $\alpha_S(m_Z) = 0.118$ . In particular  $N^n\text{LO}$  ( $n = 0, 1, 2$ ) predictions are obtained by using PDFs at the respective perturbative order and the evolution of  $\alpha_S$  at  $(n+1)$ -loop order, as provided by the PDF set. Our reference choice for renormalization ( $\mu_R$ ) and factorization ( $\mu_F$ ) scales

<sup>4</sup>In the NNLO calculation the  $\mathcal{O}(\alpha_S)$  contributions are evaluated by using Catani-Seymour subtraction.

<sup>5</sup>The numerical effect of the CKM matrix up to NLO is to reduce the cross section by less than 1%. K-factors are generally affected below the numerical uncertainties.



	definition of the fiducial volume for $pp \rightarrow \ell'^{\pm} \nu_{\ell'} \ell^+ \ell^- + X$ , $\ell, \ell' \in \{e, \mu\}$
ATLAS 8/13 TeV (cf. refs. [6, 7])	$p_{T, \ell_z} > 15 \text{ GeV}, \quad p_{T, \ell_w} > 20 \text{ GeV}, \quad  \eta_{\ell}  < 2.5,$ $ m_{\ell_z \ell_z} - m_Z  < 10 \text{ GeV}, \quad m_{T, W} > 30 \text{ GeV}, \quad \Delta R_{\ell_z \ell_z} > 0.2, \quad \Delta R_{\ell_z \ell_w} > 0.3$
CMS 13 TeV (cf. ref. [8])	$p_{T, \ell_{z,1}} > 20 \text{ GeV}, \quad p_{T, \ell_{z,2}} > 10 \text{ GeV}, \quad p_{T, \ell_w} > 20 \text{ GeV}, \quad  \eta_{\ell}  < 2.5,$ $60 \text{ GeV} < m_{\ell_z \ell_z} < 120 \text{ GeV}, \quad m_{\ell^+ \ell^-} > 4 \text{ GeV}$

**Table 1.** Definition of the fiducial volume of the  $W^{\pm}Z$  measurements by ATLAS and CMS. While  $\ell$  and  $\ell'$  refer to all charged leptons,  $\ell_z$  and  $\ell_w$  denote the leptons assigned to the  $Z$  and  $W$  boson decay, according to the procedure described in the text. Numbers in indices refer to  $p_T$ -ordered particles of the respective group.

is  $\mu_R = \mu_F = \mu_0 \equiv \frac{1}{2}(m_Z + m_W) = 85.7863 \text{ GeV}$ . Uncertainties from missing higher-order contributions are estimated as usual by independently varying  $\mu_R$  and  $\mu_F$  in the range  $0.5\mu_0 \leq \mu_R, \mu_F \leq 2\mu_0$ , with the constraint  $0.5 \leq \mu_R/\mu_F \leq 2$ . We note that a fixed scale choice is only adequate as long as the scales in the kinematic distributions do not become too large, which is indeed the case in the fiducial phase-space regions of  $W^{\pm}Z$  measurements (see sections 3.1 and 3.2). As background in new-physics searches, on the other hand, that typically focus on the high- $p_T$  tails of distributions, a dynamic scale is more appropriate, as discussed and applied in section 3.3.<sup>6</sup>

### 3.1 Fiducial cross sections

We start the presentation of our results by considering fiducial cross sections. We compute the  $W^{\pm}Z$  cross section up to NNLO in the same phase space defined by the LHC experiments and compare our results with ATLAS data at 8 [6] and 13 TeV [7], and with CMS data at 13 TeV [8]. The selection cuts defining the ATLAS and CMS fiducial volumes are summarized in table 1.

The fiducial cuts used by ATLAS are identical at both collider energies, and they are close to the applied event-selection cuts [6, 7]. The cuts require an identification of the leptons stemming from the  $Z$  and  $W$  bosons. This is trivial in the DF channel, where they are unambiguously assigned to the parent boson. In the SF channel, there are, in a theoretical computation of  $\ell\ell\ell\nu$  production, two possible combinations of opposite-sign leptons that can be matched to the  $Z$  boson. ATLAS applies the so-called resonant-shape procedure [6], where, among the two possible assignments, the one that maximizes the estimator

$$P = \left| \frac{1}{m_{\ell\ell}^2 - m_Z^2 + i\Gamma_Z m_Z} \right|^2 \cdot \left| \frac{1}{m_{\ell'\nu_{\ell'}}^2 - m_W^2 + i\Gamma_W m_W} \right|^2 \quad (3.1)$$

<sup>6</sup>In  $W^{\pm}Z$  measurements the tails of the  $p_{T,Z}$  and  $m_{T,WZ}$  (see eq. (3.3)) distributions are particularly sensitive to triple-gauge couplings. In such high- $p_T$  regions, where also EW corrections play a non-negligible role, the choice of a dynamical scale turns out to be more appropriate. The extraction of the triple-gauge couplings, however, is not considered in the present paper.

is chosen.<sup>7</sup> After this identification, the cuts involve standard requirements on the transverse momenta and pseudo-rapidities of the leptons as well as lepton separations in the  $R = \sqrt{\eta^2 + \phi^2}$  plane. The latter already regularize all possible divergences from collinear  $\gamma^* \rightarrow \ell^- \ell^+$  splittings by implying an effective invariant-mass cut on each OSSF lepton pair. The invariant mass of the lepton pair assigned to the  $Z$ -boson decay is further required not to deviate by more than 10 GeV from the  $Z$ -boson mass, and the transverse mass of the  $W$  boson, defined as

$$m_{T,W} = \sqrt{(E_{T,\ell_w} + E_{T,\nu_{\ell_w}})^2 - p_{T,\ell_w\nu_{\ell_w}}^2} \quad \text{with} \quad E_{T,x}^2 = m_x^2 + p_{T,x}^2, \quad (3.2)$$

is bounded from below.

A CMS measurement of the fiducial cross section is available only at 13 TeV [8]. The analysis applies a simple identification of the leptons in the SF channel by associating the lepton pair whose invariant mass is closest to the  $Z$ -boson mass with the  $Z$ -boson decay. The leptons then must meet standard requirements on their transverse momenta and pseudo-rapidities, which are chosen differently for the hardest and second-hardest lepton assigned to the  $Z$ -boson decay and for the lepton from the  $W$  boson. Additionally, the invariant mass of the lepton pair associated with the  $Z$  boson is required to be in a fixed range around the  $Z$ -boson mass. To guarantee infrared safety in the SF channel in spite of possible divergences from collinear  $\gamma^* \rightarrow \ell^- \ell^+$  splittings, this requirement is supplemented by a lower 4 GeV cut on the invariant mass of any OSSF lepton pair.

We note that the CMS selection cuts at the detector level are somewhat different from those defining the fiducial volume [8]. In particular, the invariant-mass cut on the identified lepton pair from the  $Z$  boson is much tighter than in the fiducial volume, and a  $b$ -jet veto is applied at detector level, which is absent in the definition of the fiducial phase space. As a meaningful comparison to theoretical predictions can only be pursued at the fiducial level, these differences require an extrapolation from the detector to the fiducial level, which could lead to additional theoretical uncertainties.

### 3.1.1 ATLAS 8 TeV

ATLAS presents their fiducial results split into both SF/DF channels and  $W^-Z/W^+Z$  production [6]. In table 2 we compare our theoretical predictions for the fiducial rates at LO, NLO and NNLO at 8 TeV to the measured cross sections. Since the cuts do not depend on the lepton flavour, the theoretical predictions are identical when exchanging electrons and muons, e.g.  $\sigma(\mu^+ \nu_\mu e^+ e^-) \equiv \sigma(e^+ \nu_e \mu^+ \mu^-)$ . The statistical uncertainties of the experimental results are strongly reduced upon combination, from  $\sim 5\% - 10\%$  for the individual channels to  $3\% - 4\%$  when combined.

For proton-proton collisions the cross sections in the  $W^+Z$  and  $W^-Z$  channels are different due to their charge-conjugate partonic initial states: the  $W^+Z$  final state is mainly produced through  $u\bar{d}$  scattering (see figure 1), while  $W^-Z$  originates from  $\bar{u}d$  scattering.

---

<sup>7</sup>We note that this definition requires the knowledge of the longitudinal component of the neutrino momentum. This variable can of course be used in the theoretical calculation, but cannot be directly extracted in the experimental analysis, and must be reconstructed with the Monte Carlo.

channel	$\sigma_{\text{LO}}$ [fb]	$\sigma_{\text{NLO}}$ [fb]	$\sigma_{\text{NNLO}}$ [fb]	$\sigma_{\text{ATLAS}}$ [fb]
$\mu^+e^+e^-$	$11.59(0)^{+2.2\%}_{-3.0\%}$	$20.42(0)^{+5.3\%}_{-4.0\%}$	$22.11(1)^{+1.8\%}_{-1.9\%}$	$23.9 \pm 6.5\%(\text{stat}) \pm 2.5\%(\text{syst}) \pm 2.2\%(\text{lumi})$
$e^+\mu^+\mu^-$				$19.9 \pm 7.2\%(\text{stat}) \pm 3.5\%(\text{syst}) \pm 2.2\%(\text{lumi})$
$e^+e^+e^-$	$11.62(0)^{+2.2\%}_{-3.0\%}$	$20.48(0)^{+5.3\%}_{-4.0\%}$	$22.17(1)^{+1.8\%}_{-1.9\%}$	$22.6 \pm 8.0\%(\text{stat}) \pm 4.4\%(\text{syst}) \pm 2.2\%(\text{lumi})$
$\mu^+\mu^+\mu^-$				$19.8 \pm 6.0\%(\text{stat}) \pm 2.5\%(\text{syst}) \pm 2.2\%(\text{lumi})$
combined	$11.60(0)^{+2.2\%}_{-3.0\%}$	$20.45(0)^{+5.3\%}_{-4.0\%}$	$22.14(1)^{+1.8\%}_{-1.9\%}$	$21.2 \pm 3.4\%(\text{stat}) \pm 2.3\%(\text{syst}) \pm 2.2\%(\text{lumi})$
$\mu^-e^+e^-$	$6.732(1)^{+2.4\%}_{-3.4\%}$	$12.35(0)^{+5.7\%}_{-4.3\%}$	$13.42(1)^{+1.9\%}_{-1.9\%}$	$12.4 \pm 9.5\%(\text{stat}) \pm 3.1\%(\text{syst}) \pm 2.3\%(\text{lumi})$
$e^-\mu^+\mu^-$				$15.7 \pm 7.5\%(\text{stat}) \pm 2.8\%(\text{syst}) \pm 2.3\%(\text{lumi})$
$e^-e^+e^-$	$6.750(1)^{+2.4\%}_{-3.4\%}$	$12.38(0)^{+5.7\%}_{-4.3\%}$	$13.47(1)^{+1.9\%}_{-2.0\%}$	$15.4 \pm 9.8\%(\text{stat}) \pm 5.0\%(\text{syst}) \pm 2.3\%(\text{lumi})$
$\mu^-\mu^+\mu^-$				$13.4 \pm 7.5\%(\text{stat}) \pm 2.8\%(\text{syst}) \pm 2.3\%(\text{lumi})$
combined	$6.741(1)^{+2.4\%}_{-3.4\%}$	$12.36(0)^{+5.7\%}_{-4.3\%}$	$13.45(1)^{+1.9\%}_{-2.0\%}$	$14.0 \pm 4.3\%(\text{stat}) \pm 2.8\%(\text{syst}) \pm 2.3\%(\text{lumi})$
$\mu^\pm e^+e^-$	$18.32(0)^{+2.3\%}_{-3.2\%}$	$32.76(1)^{+5.4\%}_{-4.1\%}$	$35.53(2)^{+1.8\%}_{-1.9\%}$	$36.3 \pm 5.4\%(\text{stat}) \pm 2.6\%(\text{syst}) \pm 2.2\%(\text{lumi})$
$e^\pm\mu^+\mu^-$				$35.7 \pm 5.3\%(\text{stat}) \pm 3.7\%(\text{syst}) \pm 2.2\%(\text{lumi})$
$e^\pm e^+e^-$	$18.37(0)^{+2.3\%}_{-3.2\%}$	$32.85(1)^{+5.4\%}_{-4.1\%}$	$35.64(2)^{+1.8\%}_{-1.9\%}$	$38.1 \pm 6.2\%(\text{stat}) \pm 4.5\%(\text{syst}) \pm 2.2\%(\text{lumi})$
$\mu^\pm\mu^+\mu^-$				$33.3 \pm 4.7\%(\text{stat}) \pm 2.5\%(\text{syst}) \pm 2.2\%(\text{lumi})$
combined	$18.35(0)^{+2.3\%}_{-3.2\%}$	$32.81(1)^{+5.4\%}_{-4.1\%}$	$35.59(2)^{+1.8\%}_{-1.9\%}$	$35.1 \pm 2.7\%(\text{stat}) \pm 2.4\%(\text{syst}) \pm 2.2\%(\text{lumi})$

**Table 2.** Fiducial cross sections for ATLAS 8 TeV. Note that due to the flavour-unspecific lepton cuts the theoretical predictions are flavour-blind, which is why the results are symmetric under  $e \leftrightarrow \mu$  exchange. The available ATLAS data from ref. [6] are also shown. “Combined” refers to the *average* of different lepton channels.

Roughly speaking, the  $u$  valence density is larger than the  $d$  valence density and  $\bar{u} \sim \bar{d}$ , so we have  $\sigma_{W^+Z} > \sigma_{W^-Z}$ .

It is clear from table 2 that the inclusion of higher-order corrections is crucial for a proper prediction of the fiducial cross sections. NLO corrections have the effect of increasing the corresponding LO results by up to 85%, and the NNLO effects further increase the NLO result by about 10%. The LO cross section is thus increased by almost a factor of two upon inclusion of higher-order corrections. The scale uncertainties are reduced from about 4% – 6% at NLO to only about 2% at NNLO. The inclusion of NNLO corrections nicely improves the agreement between the theoretical predictions and the data, which are largely consistent within the uncertainties.

These observations are irrespective of whether  $W^+Z$ ,  $W^-Z$  or their combination is considered, and very similar to what has been found for the total inclusive cross sections in ref. [18]. As pointed out there, the origin of the large radiative corrections is an approximate radiation zero [43]: the LO cross section in the leading helicity amplitude vanishes at a specific scattering angle of the  $W$  boson in the centre-of-mass frame. This phase-space region is filled only upon inclusion of higher-order contributions, thereby effectively decreasing the perturbative accuracy in that region by one order. Therefore, the perturbative uncertainties at LO and NLO, estimated from scale variations, fail to cover the actual size of

missing higher-order corrections. Nonetheless, the convergence of the perturbative series is noticeably improved beyond LO, and we expect NNLO scale uncertainties to provide the correct size of yet uncalculated perturbative contributions.

### 3.1.2 ATLAS 13 TeV

ATLAS has reported experimental results of the fiducial  $W^\pm Z$  cross section also for the early 13 TeV data set collected in 2015 [7]. At the level of the inclusive cross section very good agreement with our NNLO computation of ref. [18] is quoted. Table 3 confirms that agreement also for the fiducial cross sections. There is also a marked improvement of the accuracy of the NNLO cross section regarding its scale uncertainties, which have been reduced to  $\sim 2\%$  from  $\sim 4\% - 6\%$  at NLO. Overall, the findings at 13 TeV draw essentially the same picture as those at 8 TeV discussed in the previous section.

### 3.1.3 CMS 13 TeV

CMS provides a cross-section measurement in the fiducial phase space for  $W^\pm Z$  production only for their 13 TeV analysis, and summed over all individual lepton channels [8].<sup>8</sup> Table 4 contains our theoretical predictions at LO, NLO and NNLO for the combination of all leptonic channels. The cuts are looser as compared to the ones applied by ATLAS, but the relative size of radiative corrections is rather similar. The comparison to the fiducial cross section measured by CMS shows quite a large discrepancy: the theoretical prediction is  $2.6\sigma$  above the experimental result. We point out that CMS uses fiducial cuts that are quite different from those used in their event-selection. This comes at the price that the extrapolation from the CMS selection cuts to the fiducial phase space is affected by an uncertainty from the employed Monte Carlo generator. The observed discrepancy, however, might well be due to a statistical fluctuation of the limited dataset used in this early measurement. Further data collection at 13 TeV will hopefully clarify this issue.

## 3.2 Distributions in the fiducial phase space

We now turn to the discussion of differential observables in the fiducial phase space. In figures 3–6 we consider predictions up to NNLO accuracy for various distributions that have been measured by ATLAS at 8 TeV [6]. The fiducial phase-space definition is discussed in section 3.1, see also table 1. All figures have the identical layout: the main frame shows the predictions at LO (black dotted histogram), NLO (red dashed histogram) and NNLO (blue solid histogram) with their absolute normalization as cross section per bin (i.e. the sum of the bins is equal to the fiducial cross section), compared to the cross sections measured by ATLAS (green data points with error bars). The lower panel displays the respective bin-by-bin ratios normalized to the NLO prediction (LO is not shown here). The shaded uncertainty bands of the theoretical predictions correspond to scale variations as discussed above, and the error bars are the combined experimental uncertainties quoted

<sup>8</sup>The 8 TeV  $W^\pm Z$  measurement by CMS [5] does not provide fiducial cross sections, and the differential results are extrapolated to the full phase space. Since such results depend on the underlying Monte Carlo used for the extrapolation, we refrain from including them in our comparison. The full set of predictions for all individual channels for CMS at 8 TeV and 13 TeV are reported in appendix A.

channel	$\sigma_{\text{LO}}$ [fb]	$\sigma_{\text{NLO}}$ [fb]	$\sigma_{\text{NNLO}}$ [fb]	$\sigma_{\text{ATLAS}}$ [fb]
$\mu^+e^+e^-$	$17.33(0)^{+5.3\%}_{-6.3\%}$	$34.12(1)^{+5.3\%}_{-4.3\%}$	$37.75(2)^{+2.3\%}_{-2.0\%}$	$32.2 \pm 14.4\%(\text{stat}) \pm 5.0\%(\text{syst}) \pm 2.4\%(\text{lumi})$
$e^+\mu^+\mu^-$				$45.0 \pm 12.1\%(\text{stat}) \pm 4.6\%(\text{syst}) \pm 2.3\%(\text{lumi})$
$e^+e^+e^-$	$17.37(0)^{+5.3\%}_{-6.3\%}$	$34.21(1)^{+5.3\%}_{-4.3\%}$	$37.84(2)^{+2.2\%}_{-2.0\%}$	$28.0 \pm 19.2\%(\text{stat}) \pm 11.2\%(\text{syst}) \pm 2.4\%(\text{lumi})$
$\mu^+\mu^+\mu^-$				$36.5 \pm 11.6\%(\text{stat}) \pm 4.1\%(\text{syst}) \pm 2.3\%(\text{lumi})$
combined	$17.35(0)^{+5.3\%}_{-6.3\%}$	$34.16(1)^{+5.3\%}_{-4.3\%}$	$37.80(2)^{+2.2\%}_{-2.0\%}$	$36.7 \pm 6.7\%(\text{stat}) \pm 3.9\%(\text{syst}) \pm 2.3\%(\text{lumi})$
$\mu^-e^+e^-$	$11.50(0)^{+5.7\%}_{-6.8\%}$	$23.57(1)^{+5.5\%}_{-4.5\%}$	$26.18(1)^{+2.3\%}_{-2.1\%}$	$22.9 \pm 17.5\%(\text{stat}) \pm 5.8\%(\text{syst}) \pm 2.4\%(\text{lumi})$
$e^-\mu^+\mu^-$				$30.2 \pm 15.2\%(\text{stat}) \pm 6.9\%(\text{syst}) \pm 2.3\%(\text{lumi})$
$e^-e^+e^-$	$11.53(0)^{+5.7\%}_{-6.8\%}$	$23.63(0)^{+5.5\%}_{-4.5\%}$	$26.25(1)^{+2.2\%}_{-2.1\%}$	$22.5 \pm 21.0\%(\text{stat}) \pm 10.5\%(\text{syst}) \pm 2.4\%(\text{lumi})$
$\mu^-\mu^+\mu^-$				$27.1 \pm 13.7\%(\text{stat}) \pm 5.0\%(\text{syst}) \pm 2.4\%(\text{lumi})$
combined	$11.51(0)^{+5.7\%}_{-6.8\%}$	$23.60(1)^{+5.5\%}_{-4.5\%}$	$26.22(1)^{+2.3\%}_{-2.1\%}$	$26.1 \pm 8.1\%(\text{stat}) \pm 4.7\%(\text{syst}) \pm 2.4\%(\text{lumi})$
$\mu^\pm e^+e^-$	$28.83(0)^{+5.4\%}_{-6.5\%}$	$57.69(1)^{+5.4\%}_{-4.3\%}$	$63.93(3)^{+2.3\%}_{-2.1\%}$	$55.1 \pm 11.1\%(\text{stat}) \pm 5.1\%(\text{syst}) \pm 2.4\%(\text{lumi})$
$e^\pm\mu^+\mu^-$				$75.2 \pm 9.5\%(\text{stat}) \pm 5.3\%(\text{syst}) \pm 2.3\%(\text{lumi})$
$e^\pm e^+e^-$	$28.90(0)^{+5.4\%}_{-6.5\%}$	$57.84(1)^{+5.4\%}_{-4.3\%}$	$64.09(3)^{+2.2\%}_{-2.1\%}$	$50.5 \pm 14.2\%(\text{stat}) \pm 10.6\%(\text{syst}) \pm 2.4\%(\text{lumi})$
$\mu^\pm\mu^+\mu^-$				$63.6 \pm 8.9\%(\text{stat}) \pm 4.1\%(\text{syst}) \pm 2.3\%(\text{lumi})$
combined	$28.86(0)^{+5.4\%}_{-6.5\%}$	$57.76(1)^{+5.4\%}_{-4.3\%}$	$64.01(3)^{+2.3\%}_{-2.1\%}$	$63.2 \pm 5.2\%(\text{stat}) \pm 4.1\%(\text{syst}) \pm 2.4\%(\text{lumi})$

**Table 3.** Fiducial cross sections for ATLAS 13 TeV. Note that due to the flavour-unspecific lepton cuts the theoretical predictions are flavour-blind, which is why the results are symmetric under  $e \leftrightarrow \mu$  exchange. The available ATLAS data from ref. [7] are also shown. “Combined” refers to the *average* of different lepton channels.

channel	$\sigma_{\text{LO}}$ [fb]	$\sigma_{\text{NLO}}$ [fb]	$\sigma_{\text{NNLO}}$ [fb]	$\sigma_{\text{CMS}}$ [fb]
combined	$148.4(0)^{+5.4\%}_{-6.4\%}$	$301.4(1)^{+5.5\%}_{-4.5\%}$	$334.3(2)^{+2.3\%}_{-2.1\%}$	$258 \pm 8.1\%(\text{stat})^{+7.4\%}_{-7.7\%}(\text{syst}) \pm 3.1(\text{lumi})$

**Table 4.** Fiducial cross sections for CMS 13 TeV. The available CMS data from ref. [8] are also shown. “Combined” refers to the *sum* of all separate contributions. Our theoretical predictions for all individual channels for CMS at 8 TeV and 13 TeV can be found in appendix A.

by ATLAS. Unless stated otherwise, all distributions include the combination of all relevant leptonic channels (SF/DF channels and  $W^+Z/W^-Z$  production). Note that, in order to compare to ATLAS results, we combine different lepton channels by averaging them for both the fiducial cross sections and distributions, while summing the cross sections for  $W^+Z$  and  $W^-Z$  production.

Some general statements regarding the scale uncertainties which are common to all subsequent plots are in order: NNLO corrections further reduce the scale dependence of the NLO cross sections in all distributions. In absolute terms, the NLO uncertainties generally vary within 5%–10%, and reach up to 20% only in the tails of some transverse-momentum distributions. The NNLO uncertainties, on the other hand, hardly ever exceed 5% in all differential observables. Correspondingly, given that the NNLO corrections on the fiducial rate are about +8.5%, NLO and NNLO scale-uncertainty bands mostly do not

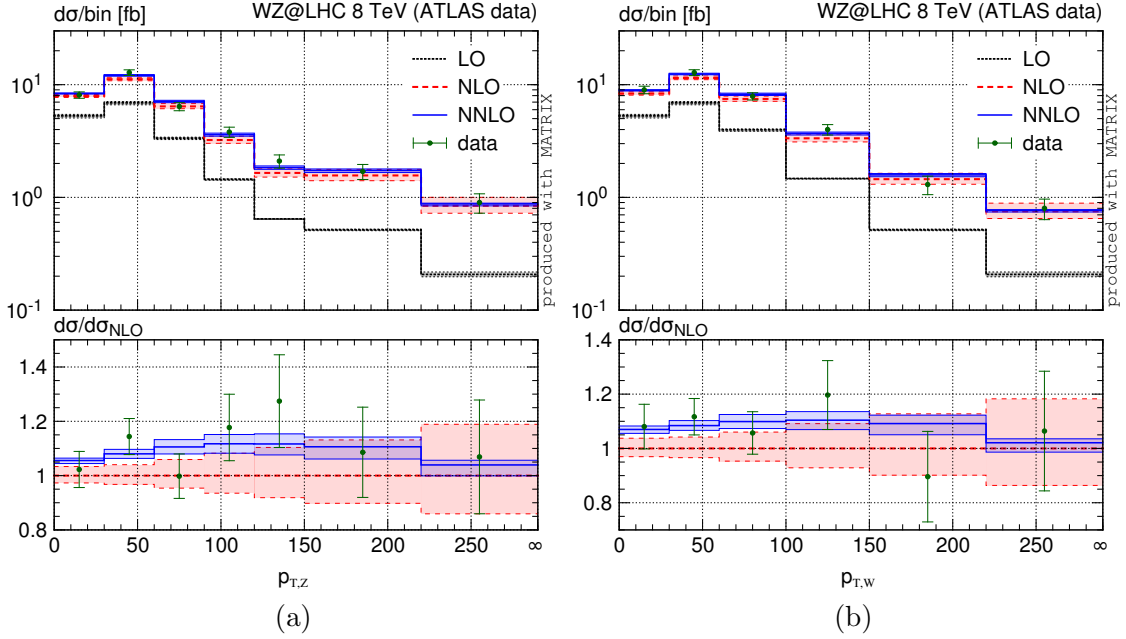


**Figure 3.** Distribution in the transverse momentum of the reconstructed (a)  $Z$  and (b)  $W$  bosons at LO (black, dotted), NLO (red, dashed) and NNLO (blue, solid) compared to the corresponding ATLAS data at 8 TeV (green points with error bars). The lower panel shows the ratio over the NLO prediction.

overlap, in particular in the bins that provide the bulk of the cross section. Nonetheless, we expect NNLO uncertainties to generally provide the correct size of missing higher-order contributions (see our corresponding comments at the end of section 3.1.1).

Figure 3 shows the transverse-momentum spectra of the reconstructed  $Z$  and  $W$  bosons, which both peak around  $p_{T,V} \sim 30$  GeV. As can be seen from the ratio plots, the inclusion of NNLO corrections affects the shapes of both distributions at the 10% level, the effect being largest in the region  $p_{T,V} \lesssim 150$  GeV. The comparison with the data is good already at NLO, but it is further improved, in particular in terms of shape, at NNLO. All data points agree within roughly  $1\sigma$  with the NNLO predictions.

In figure 4(a), we consider the distribution in the transverse mass of the  $WZ$  system, defined by

$$m_{T,WZ} = \sqrt{\left(E_{T,\ell_w} + E_{T,\nu_{\ell_w}} + E_{T,\ell_z^+} + E_{T,\ell_z^-}\right)^2 - p_{T,\ell_w\nu_{\ell_w}\ell_z^+\ell_z^-}^2} \quad \text{with} \quad E_{T,x}^2 = m_x^2 + p_{T,x}^2. \quad (3.3)$$

With shape effects of about 15%, the NNLO corrections significantly soften the spectrum. Already the NLO prediction is in good agreement with data, and the NNLO corrections tend to slightly improve that agreement mainly due to the shape correction, so that the measured results are well described by the theoretical predictions within roughly  $1\sigma$  of the experimental errors.

The ATLAS result for the missing transverse energy distribution in figure 4(b) shows some discrepancy in shape compared to the NLO prediction. The NNLO corrections are

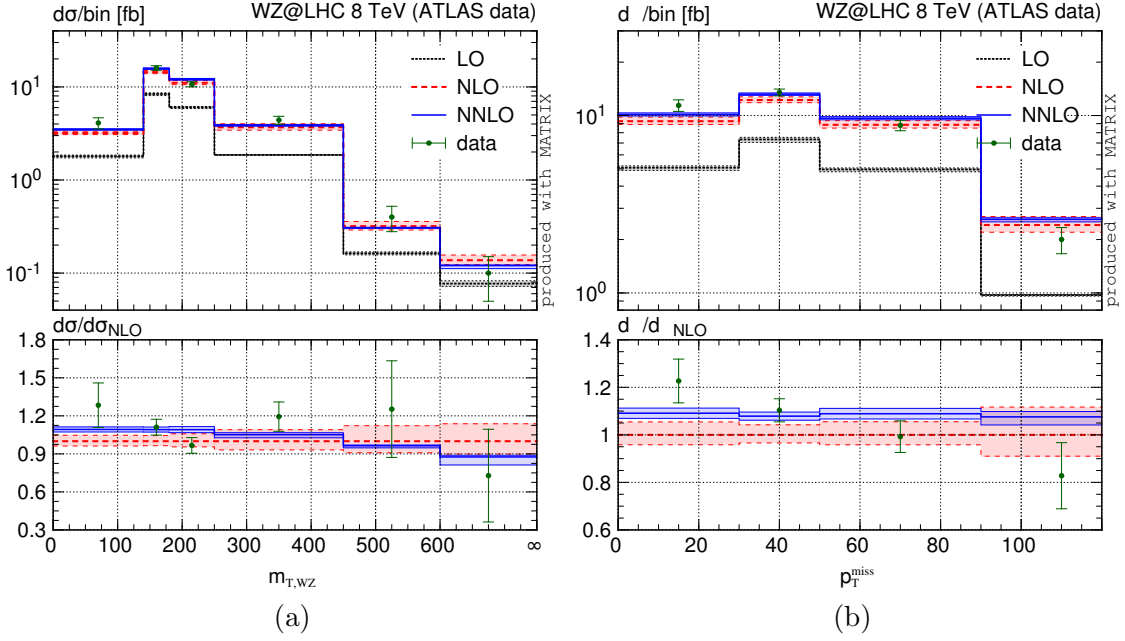


**Figure 4.** Same as figure 3, but for (a) the transverse mass of the  $WZ$  system as defined in eq. (3.3) and (b) the missing transverse energy.

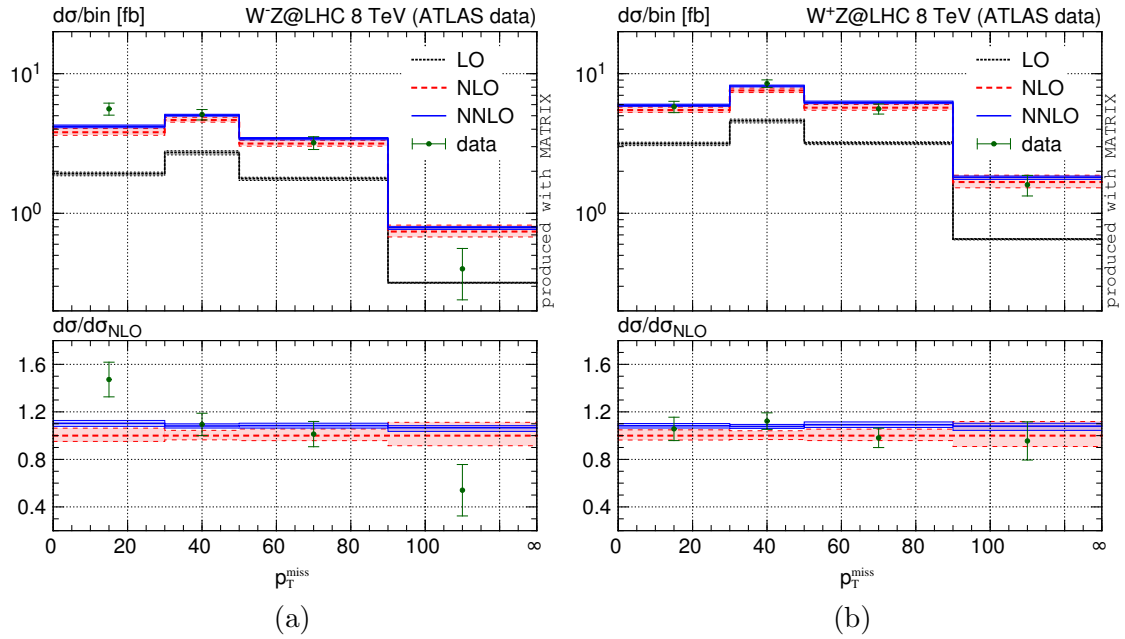


**Figure 5.** Same as figure 4(b), but separated by (a)  $W^-Z$  and (b)  $W^+Z$  production.

essentially flat, so they cannot account for that difference. Overall, the uncertainties of the measured results are still rather large, such that the deviation of the predicted cross section in each bin stays within  $1\sigma - 2\sigma$ . Looking at figure 5 where we plot the missing transverse energy distribution separately for  $W^-Z$  and  $W^+Z$  production, we see that the observed discrepancy between theory and data appears only for  $W^-Z$  production, where



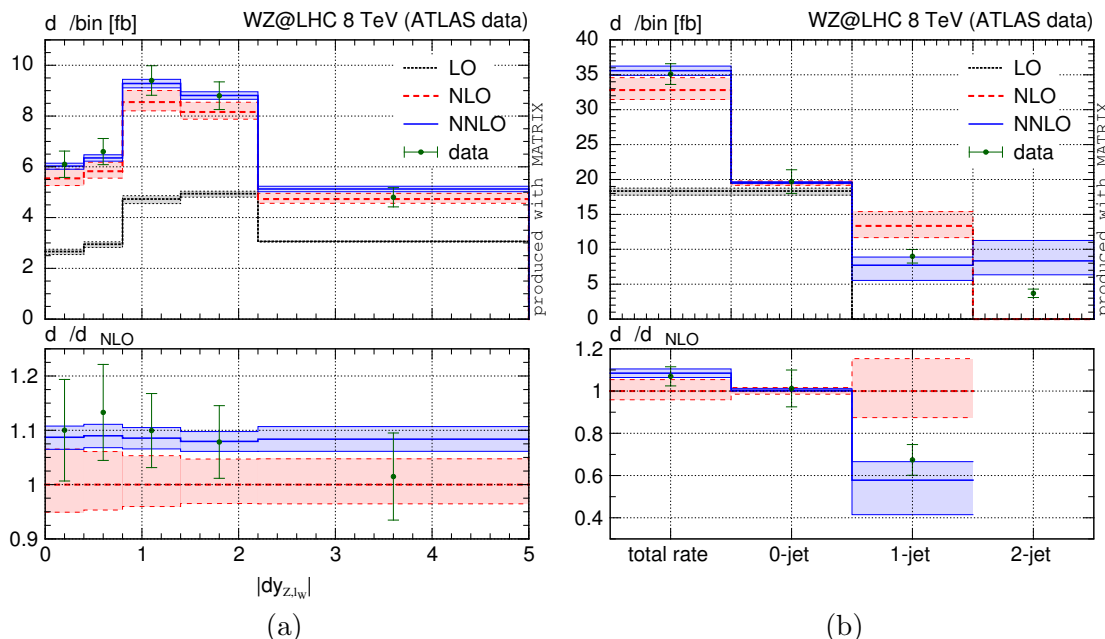


**Figure 6.** Same as figure 3, but for (a) the absolute rapidity separation between the reconstructed  $Z$  boson and the lepton from the  $W$ -boson decay, and (b) the number of jets.

it extends up to roughly  $2\sigma - 3\sigma$  for the lowest and highest  $p_T^{\text{miss}}$  bins. To clarify the origin of this discrepancy more precise data are needed, given that only four separate bins are measured at the moment.

Next, we discuss the absolute rapidity difference between the reconstructed  $Z$  boson and the lepton associated with the  $W$ -boson decay, shown in figure 6(a). This  $|dy_{Z,\ell_W}|$  distribution has a distinctive shape, with a dip at vanishing rapidity difference and a maximum around  $|dy_{Z,\ell_W}| = 0.8$ , and it is sensitive to the approximate radiation zero [43] mentioned before. As expected, the LO prediction does not describe the data in any sensible way. The NLO prediction already captures the dominant shape effects. The NNLO corrections are rather flat and are consistent within uncertainties with (and in most cases right on top of) the data, thanks to the improved normalization.

Finally, figure 6(b) shows the distribution in the jet multiplicity. Jets are defined with the anti- $k_T$  algorithm [62] with radius parameter  $R = 0.4$ . A jet must have a minimum transverse momentum of 25 GeV and a maximum pseudo-rapidity of 4.5. We already know that the measured fiducial cross section is in excellent agreement with the NNLO prediction. As expected, radiative corrections are strongly reduced when considering a jet veto (0-jet bin). NLO and NNLO predictions are essentially indistinguishable, apart from the reduction of the theoretical uncertainties when going from NLO to NNLO. The experimental result is right on top of them. In the exclusive 1-jet bin NLO (NNLO) predictions are formally only LO (NLO) accurate. It is well-known that LO-accurate predictions tend to underestimate the uncertainties. The blue solid NNLO result has the effect of decreasing the cross section in that bin by almost a factor of two with respect to NLO, well beyond the given uncertainties. The data point is significantly closer to the

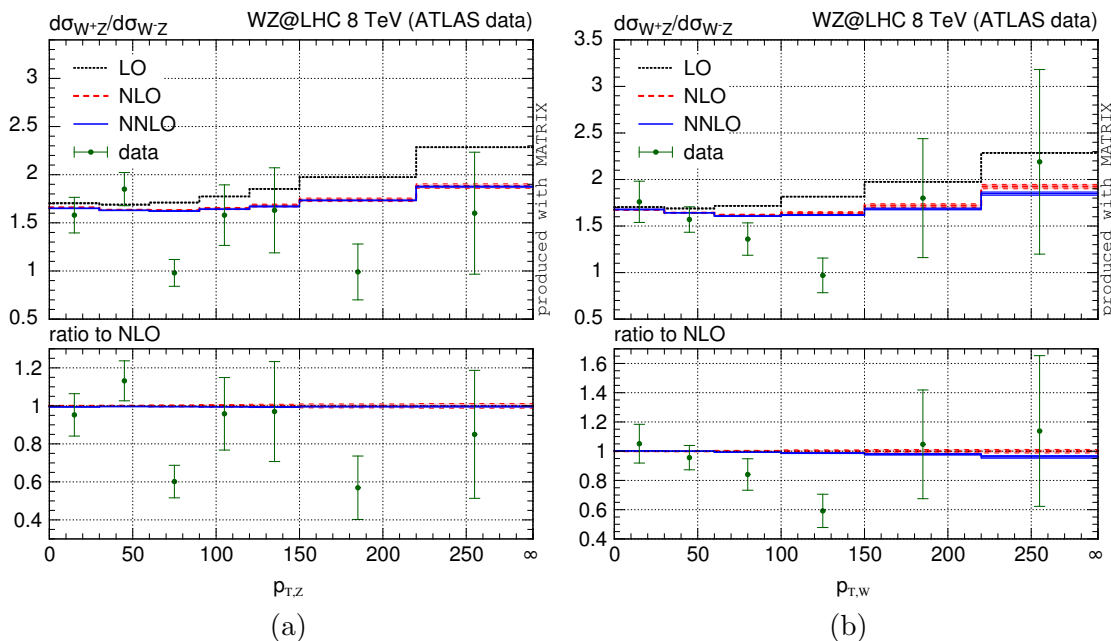


**Figure 7.** Same as figure 3, but shows the ratio of cross sections for  $W^+Z$  and  $W^-Z$  production.

NNLO prediction and fully consistent with it within uncertainties. Finally, in the 2-jet bin even the NNLO contribution is effectively only LO, and our computation cannot provide a reliable prediction. Indeed, it significantly overestimates the measured cross section. A more accurate description of the 2-jet bin requires at least NLO QCD corrections to the  $W^\pm Z + 2$  jets process [63].

We conclude our discussion of differential distributions by considering ratios of  $W^+Z$  over  $W^-Z$  cross sections. In figures 7–9 (a) such ratios are compared to the ATLAS 8 TeV data. Otherwise, these plots have exactly the same structure as the previous ones. The uncertainty bands are computed by taking fully correlated scale variations, i.e., using the same scale in numerator and denominator. The ensuing bands are extremely small, with relative uncertainties never exceeding  $\sim 1\%$ – $2\%$  both at NLO and NNLO. In most cases the perturbative computation of the ratios is very stable and in particular NNLO corrections are very small, which justifies fully correlated scale variations to estimate the perturbative uncertainties. Nevertheless, some observables are affected by  $\mathcal{O}(\alpha_S^2)$  corrections beyond the residual uncertainty bands: such cases are discussed at the end of this section.

By and large, we find reasonable agreement between the predicted and the measured ratios in all distributions under consideration, which is, in part, due to the relatively large experimental uncertainties. The latter prevent to clearly discriminate whether NNLO corrections improve the agreement with data. Nevertheless, for each distribution at least one data point deviates from the prediction by more than  $2\sigma$ , some of which appear even quite significant. For example, in figure 7 (a) there is one bin in the transverse-momentum spectrum of the reconstructed  $Z$  boson with a discrepancy of roughly  $4\sigma$  and another one with more than  $2\sigma$ . However, the experimental results fluctuate too much to claim that these are genuine effects beyond statistics. In fact, similar differences as we observe here are evident also in the ATLAS study [6] when data are compared to NLO+PS predictions.

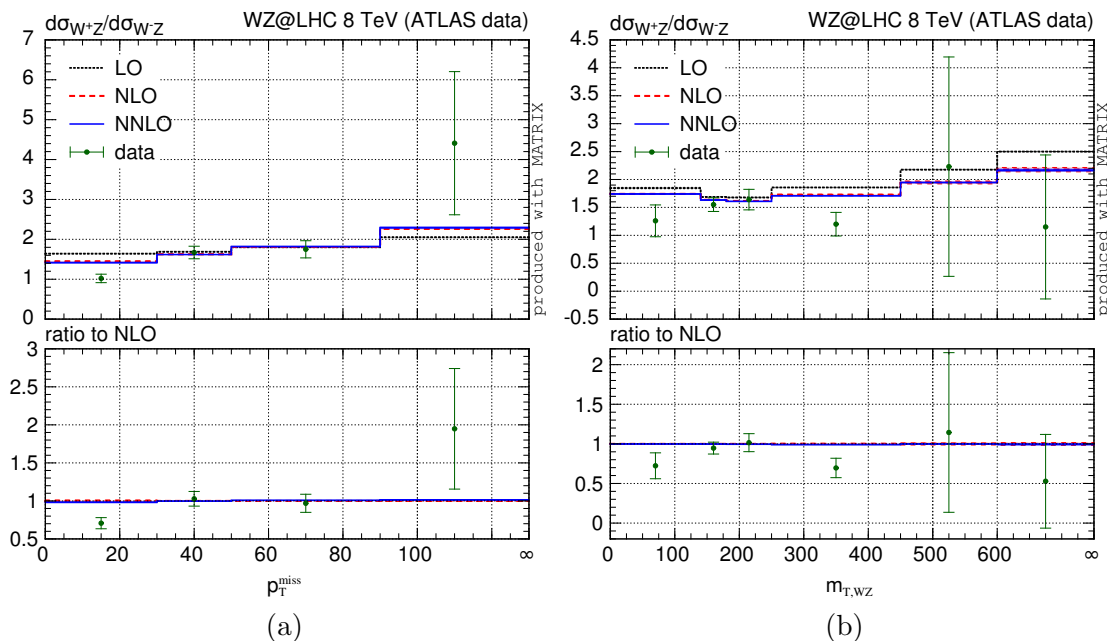


**Figure 8.** Same as figure 4, but shows the ratio of cross sections for  $W^+Z$  and  $W^-Z$  production.

Only higher experimental accuracy, to become available at 13 TeV soon, will allow for a more conclusive comparison in these cases. Indeed, even the distribution in the missing transverse energy in figure 8, where we found some apparent difference in the shape for  $W^-Z$ , but not for  $W^+Z$  production (see figure 5), does not seem to be particularly (more) significant when considering the  $W^+Z/W^-Z$  ratio due to the large experimental errors.

Finally, we point out certain distributions which show prominent shape differences between  $W^+Z$  and  $W^-Z$  production, while featuring visible effects from the NNLO corrections. Several distributions exist, see, e.g., figures 9(b)–11, which depend rather strongly on the charge of the  $W$  boson. Unfortunately, large NNLO effects often appear only in corners of phase space that are strongly suppressed and thus have low experimental sensitivity. One example is the absolute rapidity difference between the reconstructed  $Z$  boson and the lepton associated with the  $W$ -boson decay, which is compared to data in figure 9(a), but shown with a finer binning in figure 9(b): the effect of NNLO corrections in the forward region is manifest, but it is entirely due to differences between NLO and NNLO PDFs.<sup>9</sup>

There are, however, examples where the effects of NNLO corrections on the  $W^+Z/W^-Z$  ratio are evident already in the bulk region of the distribution. Such examples are given in figures 10–11. The  $W^+Z/W^-Z$  ratio for the invariant mass of the three leptons in figure 10(a) evidently increases for small  $m_{\ell\ell\ell}$  values and decreases in the tail of the distribution upon inclusion of higher-order corrections, the effect being at the 5% level. Also the  $W^+Z/W^-Z$  ratio as a function of the invariant mass of the  $W^\pm Z$  pair in figure 10(b) shows a large impact of NNLO corrections, although this is close to the kinematical boundary where the cross section is strongly suppressed.

The largest impact of NNLO corrections on the ratio of  $W^+Z$  and  $W^-Z$  cross sections is found for the distribution in the transverse momentum of the lepton associated with the

<sup>9</sup>We have checked that by using the NNLO set also for the NLO predictions the difference disappears.

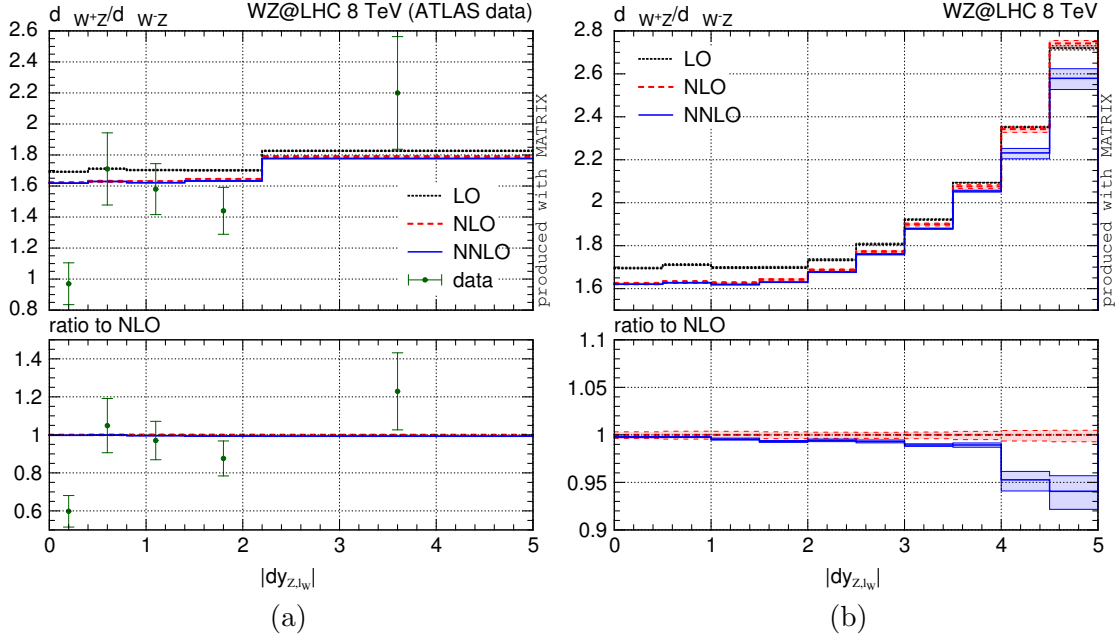


**Figure 9.** (a) Same as figure 6 (a), but shows the ratio of cross sections for  $W^+Z$  and  $W^-Z$  production, and (b) same plot with a different binning and without data.

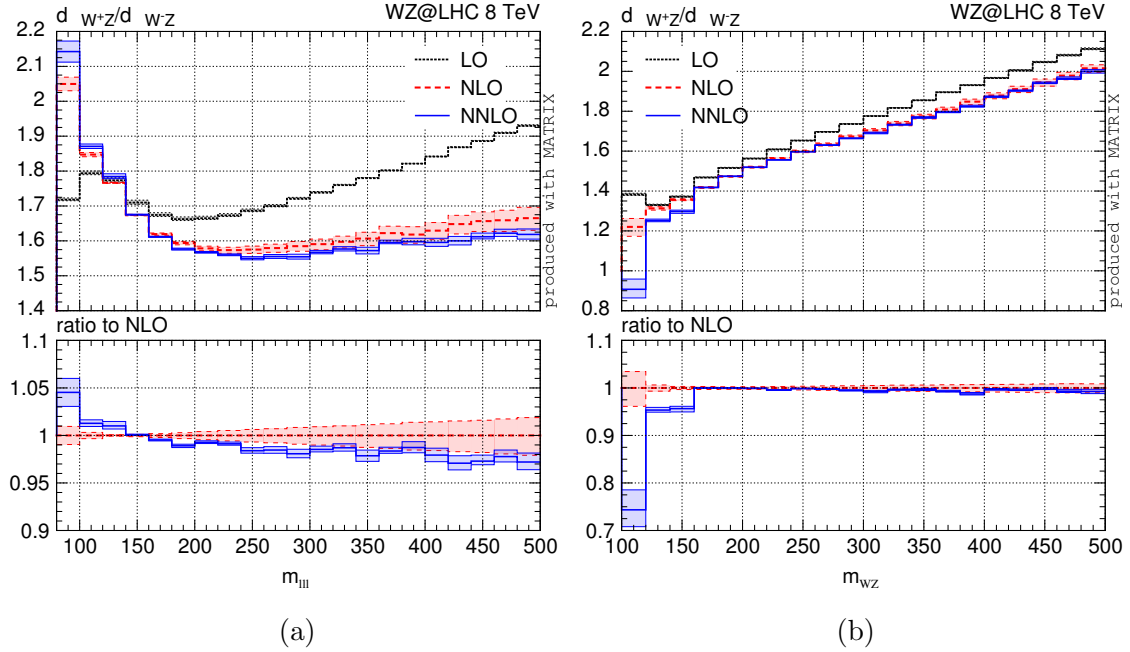


**Figure 10.** Ratio of  $W^+Z$  and  $W^-Z$  distributions in the (a) invariant mass of the three leptons and (b) invariant mass of the  $WZ$  system.

$W$ -boson decay ( $p_{T,\ell_w}$ ) in figure 11 (a). The shape of the ratio significantly changes when going from NLO to NNLO, the effects being more than 10% in the tail of the distribution. Qualitatively similar, though smaller, effects can be observed in figure 11 (b) for the leading-lepton  $p_T$ .

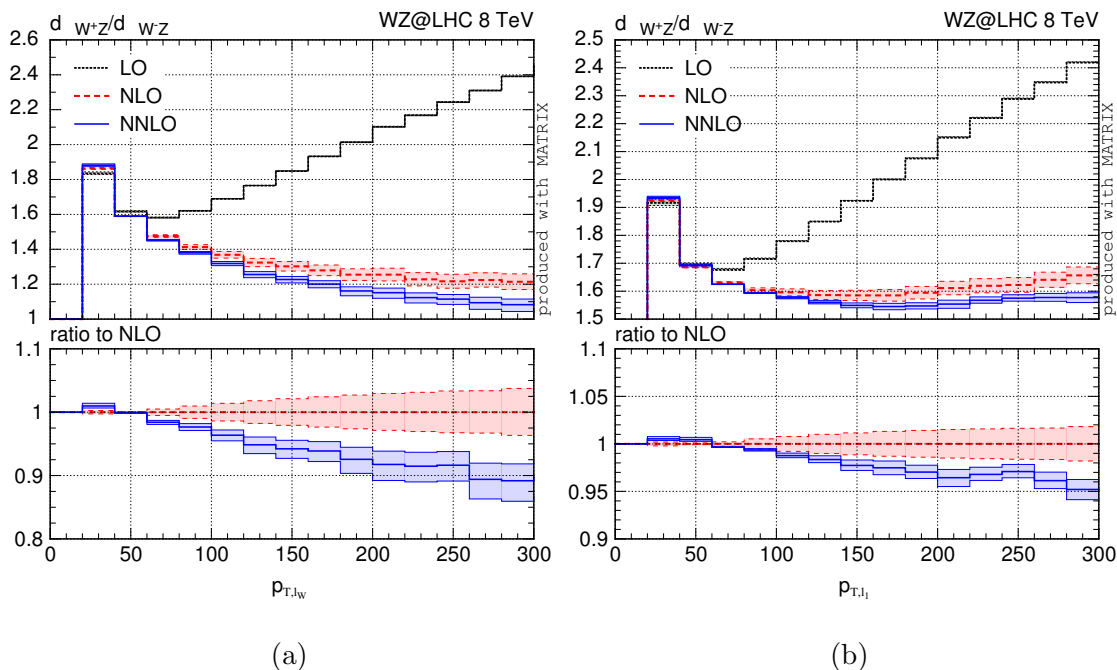


**Figure 11.** Ratio of  $W^+Z$  and  $W^-Z$  distributions in (a) the transverse momentum of the lepton associated with the  $W$  decay and (b) the transverse momentum of the hardest lepton.

We conclude our presentation of the differential distributions with a comment on the perturbative uncertainties affecting the  $W^+Z/W^-Z$  ratios. The NLO uncertainties reported in figures 10–11 underestimate the actual size of the NNLO corrections in certain phase-space regions. We note, however, that such uncertainties are computed by performing fully correlated variations. While in the majority of the cases this procedure is justified by the small size of perturbative corrections, in some phase space regions independent scale variations in numerator and denominator would be more appropriate to obtain realistic perturbative uncertainties. This is demonstrated in figure 12, which separately shows the absolute  $p_{T,\ell_w}$  distribution for  $W^+Z$  and  $W^-Z$  production. Indeed, the NLO and NNLO predictions are actually quite consistent within uncertainties. Similar conclusions can be drawn also for the other observables in figures 10–11 when separately looking at their absolute distributions for  $W^+Z$  and  $W^-Z$  production.

### 3.3 New-physics searches

In section 3.1 and section 3.2 we have presented cross sections and distributions in the fiducial regions defined by ATLAS and CMS to isolate the  $W^\pm Z$  signature. The comparison between theoretical predictions and experimental data in this region is certainly important to test the SM. The  $W^\pm Z$  signature, however, and, more precisely, the production of three leptons + missing energy, is important in many BSM searches, for which the SM prediction provides an irreducible background. One important example in this respect are searches for heavy supersymmetric (SUSY) particles: the extraction of limits on SUSY masses relies on a precise prediction of the SM background. In the following, we present an illustrative

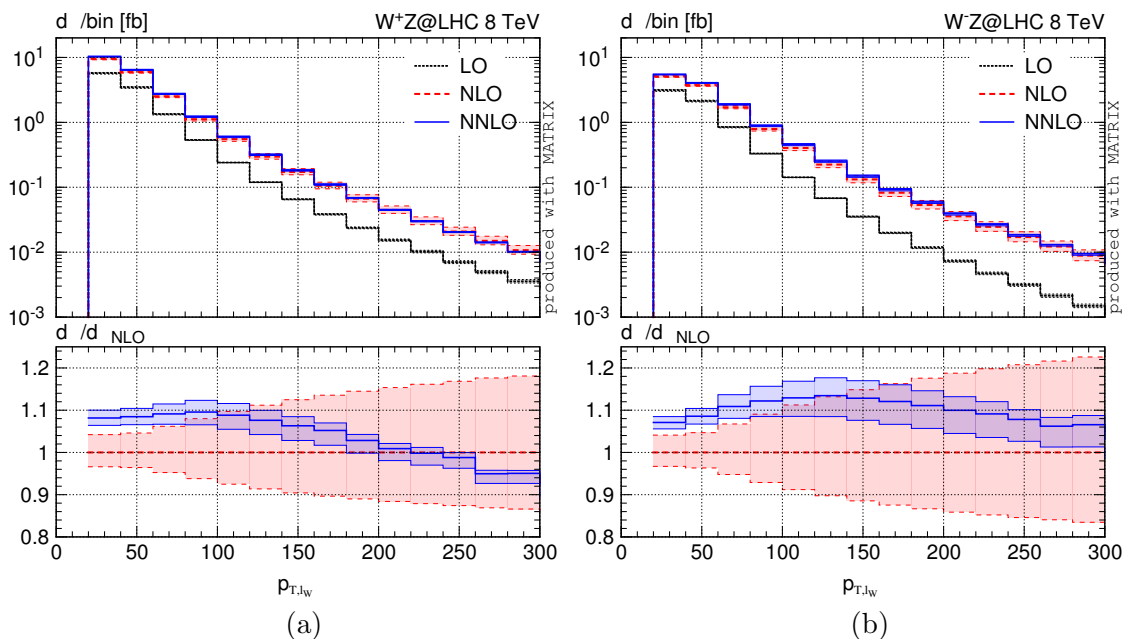


**Figure 12.** Distributions in the transverse momentum of the lepton associated with the  $W$  decay, but separately for (a)  $W^+Z$  and (b)  $W^-Z$  production (corresponding to the ratio in figure 11 (a)).

study where we focus on a definite scenario for SUSY searches, and we study the impact of higher-order QCD corrections on both cross sections and distributions.

Typical experimental new-physics searches that consider three leptons plus missing energy apply basic cuts which are rather similar to those considered in SM measurements. Here we follow as close as possible the selection cuts used in the CMS analysis of ref. [44] at 13 TeV. The selection cuts are summarized in table 5; they differ in some details from those considered in section 3.1: first of all, lepton cuts are chosen differently for electrons and muons. More precisely, all leptons are first ordered in  $p_T$ , and then the  $p_T$  threshold for each lepton is set according to its flavour and to whether it is the leading or a subleading lepton. Also the pseudo-rapidity cuts are different for electrons and muons. These cuts imply that the theoretical prediction of the cross section in this case is not symmetric under  $e \leftrightarrow \mu$  exchange any more, and the full set of eight channels must be computed separately for the  $\ell\ell\ell\nu$  final state. Furthermore, the invariant mass of the three leptons is required to differ by at least 15 GeV from the  $Z$ -boson mass, and the invariant mass of every OSSF lepton pair is bounded from below to ensure IR safety.

Our goal is to study QCD effects on distributions which are known to provide a high experimental sensitivity to isolate a SUSY signal over the SM background. The essential observables, ordered by their relevance, are:<sup>10</sup>

<sup>10</sup>We note that, contrary to the SM studies of section 3.1 and section 3.2, the cuts we consider here do not require to identify the lepton pair coming from a  $Z$  boson. A  $Z$ -boson identification is needed only for specific observables, namely  $m_{T,W}$  and  $m_{\ell\ell}$ . The identification is the same as used by the CMS SM analysis at 13 TeV, outlined in section 3.1. The OSSF lepton pair with the invariant mass closest to  $m_Z$  is associated with the  $Z$  boson.

	definition of the selection cuts for $pp \rightarrow \ell'^{\pm} \nu_{\ell'} \ell^+ \ell^- + X$ , $\ell, \ell' \in \{e, \mu\}$
CMS 13 TeV (cf. ref. [44])	$p_{T, \ell_1} > 25(20) \text{ GeV}$ if $\ell_1 = e(\mu)$ , $p_{T, \ell_1} > 25 \text{ GeV}$ if $\ell_1 = \mu$ and $\ell_{\geq 2} \neq \mu$ $p_{T, \ell_{\geq 2}} > 15(10) \text{ GeV}$ if $\ell_{\geq 2} = e(\mu)$ , $ \eta_e  < 2.5$ , $ \eta_{\mu}  < 2.4$ , $ m_{3\ell} - m_Z  > 15 \text{ GeV}$ , $m_{\ell^+ \ell^-} > 12 \text{ GeV}$

**Table 5.** Selection cuts used in our new-physics analysis.  $\ell$  and  $\ell'$  refer to all charged leptons, and numbers in indices refer to  $p_T$ -ordered particles of the respective group.

- the missing transverse energy  $p_T^{\text{miss}}$ , which (in particular in its tail) is highly sensitive if unobserved SUSY particles, usually the lightest supersymmetric particle (LSP), are produced via chargino-neutralino pair production;
- the transverse mass of the  $W$  boson  $m_{T,W}$ , more precisely of the system of missing energy and the lepton not associated with the  $Z$ -boson decay, which is to some extent complementary to  $p_T^{\text{miss}}$ ;
- the invariant mass of the lepton pair associated with the  $Z$ -boson decay  $m_{\ell\ell}$ , which allows a discrimination between searches in the SUSY parameter space with a small ( $m_{\ell\ell} \ll m_Z$ ), intermediate ( $m_{\ell\ell} \sim m_Z$ ) and large ( $m_{\ell\ell} \gg m_Z$ ) mass difference of neutralino and LSP.

Based on these considerations, we choose four different categories, which are inspired by the categories considered in ref. [44]:

- Category I:** no additional cut  
**Category II:**  $p_T^{\text{miss}} > 200 \text{ GeV}$   
**Category III:**  $m_{T,W} > 120 \text{ GeV}$   
**Category IV:**  $m_{\ell\ell} > 105 \text{ GeV}$

Our calculation is performed by using the setup discussed at the beginning of this section and employed in section 3.1 and section 3.2. However, since we are interested in studying the impact of QCD radiative corrections in a phase space region which is characterized by relatively large transverse momenta (up to  $\mathcal{O}(1 \text{ TeV})$ ), the fixed scale  $\mu_0 = \frac{1}{2}(m_Z + m_W)$  is not fully appropriate. In the present study we use instead a dynamic scale defined as

$$\mu_R = \mu_F = \mu_0 \equiv \frac{1}{2} \left( \sqrt{m_Z^2 + p_{T, \ell_z \ell_z}^2} + \sqrt{m_W^2 + p_{T, \ell_w \nu_{\ell_w}}^2} \right), \quad (3.4)$$

where  $p_{T, \ell_z \ell_z}$  and  $p_{T, \ell_w \nu_{\ell_w}}$  are the transverse-momenta of the identified  $Z$  and  $W$  bosons, respectively. In the limit of small transverse momenta eq. (3.4) reduces to the fixed scale  $\mu_0 = \frac{1}{2}(m_Z + m_W)$  used in section 3.1 and section 3.2.

In table 6 we report our results for the integrated cross sections in the four categories. Four separate results are given in that table by dividing into  $W^+Z$  and  $W^-Z$  production



as well as SF and DF channels:  $\ell'^+\ell^+\ell^-$ ,  $\ell^+\ell^+\ell^-$ ,  $\ell'^-\ell^+\ell^-$  and  $\ell^-\ell^+\ell^-$ . Throughout this section, flavour channels related by  $e \leftrightarrow \mu$  exchange are summed over and the combination of individual channels is always done by summing them. We start our discussion from Category I, for which the cross section is of the order of the fiducial cross sections presented in section 3.1 for the SM measurements at 13 TeV, although with somewhat looser selection cuts. The relative radiative correction are large: they amount to about 94% at NLO and 13% at NNLO. These relative corrections are slightly larger for  $W^-Z$  production as compared to  $W^+Z$  production as can be inferred from the separate rows in the table. Results in the SF and DF channels are of the same size.

An additional and stringent cut on the missing transverse energy of  $p_T^{\text{miss}} > 200$  GeV (Category II) changes this picture dramatically: the cross section is reduced by roughly two orders of magnitude. The LO prediction vastly underestimates the cross section, with NLO corrections of several hundred percent. These corrections are significantly larger for the  $W^+Z$  cross section ( $\sim 320\%$ ) than for  $W^-Z$  production ( $\sim 240\%$ ). This is not unexpected: a hard cut on  $p_T^{\text{miss}}$  enhances the relevance of the high- $p_T$  region, where QCD corrections are more important. Moreover, the  $W^+Z$  final state is mainly produced through  $u\bar{d}$  scattering, while  $W^-Z$  originates from  $\bar{u}d$  scattering. The  $u$  quark carries on average more momentum than the  $d$  quark, thus leading to harder  $p_T$  spectra for the  $W^+Z$  final states compared to  $W^-Z$ . Following similar arguments, also the NNLO contribution is sizeable. It is roughly 22%, which is in particular larger than in the more inclusive Category I. This clearly confirms the importance of NNLO corrections when scenarios with cuts on observables relevant to new-physics searches, such as  $p_T^{\text{miss}}$ , are under consideration.

In Category III (additional cut  $m_{T,W} > 120$  GeV), on the other hand, the cut has a rather mild effect on the NLO corrections, which are about 70%, i.e. even slightly lower than in Category I. NNLO corrections have an effect of about 8%. What turns out to be striking in this category is the difference between SF and DF channels, which are similarly large in the two previous categories. Here, the SF results are more than a factor of three higher than the corresponding DF cross section. We will discuss the origin and the implications of this observation in detail below.

QCD corrections are also very mildly affected by a high cut on  $m_{\ell\ell}$  in Category IV ( $m_{\ell\ell} > 105$  GeV) which forces the  $Z$  boson to be off-shell. The difference between SF and DF results is smaller and has the opposite sign with respect to Category III, being, however, still of order 10%–20% depending on the order.

Comparing the  $W^+Z$  and  $W^-Z$  ratios in the four categories, we see that, due to the different contributing partonic channels, they strongly depend on the applied phase-space cuts, with  $\sigma_{W^+Z}/\sigma_{W^-Z} \approx 1.47$  in Category I,  $\sigma_{W^+Z}/\sigma_{W^-Z} \approx 2.71$  in Category II,  $\sigma_{W^+Z}/\sigma_{W^-Z} \approx 1.69$  in Category III and  $\sigma_{W^+Z}/\sigma_{W^-Z} \approx 1.48$  in Category IV at NNLO. We note that the precise value of the ratio of  $W^+Z$  and  $W^-Z$  cross sections may be affected by the specific choice of the used PDFs.

Let us discuss in more detail the large difference between SF and DF cross sections in Category III. This seems surprising at first sight, since, as outlined in section 2, the SF and DF channels feature the same diagrams and have the same generic resonant structures. Indeed, all SM results as well as BSM results in Category I and II show at most minor differences between SF and DF channels. This is true both for rates and distributions.

channel	$\sigma_{\text{LO}}$ [fb]	$\sigma_{\text{NLO}}$ [fb]	$\sigma_{\text{NNLO}}$ [fb]	$\sigma_{\text{NLO}}/\sigma_{\text{LO}}-1$	$\sigma_{\text{NNLO}}/\sigma_{\text{NLO}}-1$
Category I					
$\ell'+\ell+\ell^-$	$49.45(0)^{+4.9\%}_{-5.8\%}$	$94.12(2)^{+4.8\%}_{-3.9\%}$	$105.9(1)^{+2.3\%}_{-2.2\%}$	90.3%	12.6%
$\ell+\ell+\ell^-$	$48.97(0)^{+4.8\%}_{-5.8\%}$	$93.13(2)^{+4.8\%}_{-3.9\%}$	$104.7(1)^{+2.2\%}_{-2.1\%}$	90.2%	12.4%
$\ell'-\ell+\ell^-$	$32.04(0)^{+5.3\%}_{-6.3\%}$	$63.68(3)^{+5.0\%}_{-4.1\%}$	$71.89(4)^{+2.3\%}_{-2.2\%}$	98.7%	12.9%
$\ell-\ell+\ell^-$	$31.74(0)^{+5.3\%}_{-6.3\%}$	$63.00(2)^{+5.0\%}_{-4.1\%}$	$71.13(4)^{+2.2\%}_{-2.2\%}$	98.5%	12.9%
combined	$162.2(0)^{+5.0\%}_{-6.0\%}$	$313.9(1)^{+4.9\%}_{-4.0\%}$	$353.7(3)^{+2.2\%}_{-2.2\%}$	93.5%	12.7%
Category II					
$\ell'+\ell+\ell^-$	$0.3482(0)^{+2.8\%}_{-2.8\%}$	$1.456(0)^{+13\%}_{-11\%}$	$1.799(1)^{+5.2\%}_{-5.4\%}$	318%	23.6%
$\ell+\ell+\ell^-$	$0.3486(0)^{+2.8\%}_{-2.8\%}$	$1.452(0)^{+13\%}_{-11\%}$	$1.789(1)^{+5.1\%}_{-5.4\%}$	316%	23.2%
$\ell'-\ell+\ell^-$	$0.1644(0)^{+2.6\%}_{-2.7\%}$	$0.5546(1)^{+12\%}_{-9.9\%}$	$0.6631(4)^{+4.3\%}_{-4.8\%}$	237%	19.6%
$\ell-\ell+\ell^-$	$0.1645(0)^{+2.6\%}_{-2.7\%}$	$0.5535(1)^{+12\%}_{-9.9\%}$	$0.6600(3)^{+4.2\%}_{-4.7\%}$	237%	19.2%
combined	$1.026(0)^{+2.7\%}_{-2.8\%}$	$4.015(1)^{+13\%}_{-10\%}$	$4.911(3)^{+4.9\%}_{-5.2\%}$	292%	22.3%
Category III					
$\ell'+\ell+\ell^-$	$0.3642(0)^{+1.5\%}_{-2.2\%}$	$0.5909(1)^{+4.3\%}_{-3.3\%}$	$0.6373(16)^{+1.6\%}_{-1.6\%}$	62.3%	7.86%
$\ell+\ell+\ell^-$	$1.090(0)^{+1.7\%}_{-2.4\%}$	$1.904(0)^{+4.8\%}_{-3.8\%}$	$2.071(2)^{+1.9\%}_{-1.9\%}$	74.7%	8.79%
$\ell'-\ell+\ell^-$	$0.2055(0)^{+2.0\%}_{-2.8\%}$	$0.3447(1)^{+4.5\%}_{-3.4\%}$	$0.3731(9)^{+1.6\%}_{-1.7\%}$	67.8%	8.22%
$\ell-\ell+\ell^-$	$0.6463(1)^{+2.1\%}_{-2.9\%}$	$1.136(0)^{+4.8\%}_{-3.7\%}$	$1.232(1)^{+1.7\%}_{-1.7\%}$	75.8%	8.42%
combined	$2.306(0)^{+1.8\%}_{-2.5\%}$	$3.976(1)^{+4.7\%}_{-3.7\%}$	$4.313(6)^{+1.8\%}_{-1.8\%}$	72.4%	8.50%
Category IV					
$\ell'+\ell+\ell^-$	$2.500(0)^{+3.1\%}_{-3.9\%}$	$4.299(1)^{+4.1\%}_{-3.4\%}$	$4.682(2)^{+1.7\%}_{-1.6\%}$	72.0%	8.92%
$\ell+\ell+\ell^-$	$2.063(0)^{+3.4\%}_{-4.2\%}$	$3.740(1)^{+4.5\%}_{-3.6\%}$	$4.160(2)^{+2.2\%}_{-2.0\%}$	81.3%	11.2%
$\ell'-\ell+\ell^-$	$1.603(0)^{+3.4\%}_{-4.4\%}$	$2.805(1)^{+4.2\%}_{-3.5\%}$	$3.058(1)^{+1.7\%}_{-1.6\%}$	75.0%	9.01%
$\ell-\ell+\ell^-$	$1.373(0)^{+3.8\%}_{-4.7\%}$	$2.591(1)^{+4.7\%}_{-3.9\%}$	$2.904(1)^{+2.2\%}_{-2.1\%}$	88.7%	12.1%
combined	$7.540(1)^{+3.4\%}_{-4.2\%}$	$13.44(0)^{+4.4\%}_{-3.6\%}$	$14.80(1)^{+1.9\%}_{-1.8\%}$	78.2%	10.2%

**Table 6.** Fiducial cross sections at LO, NLO and NNLO for all three categories split by SF ( $\ell\ell\ell$ ) and DF ( $\ell'\ell\ell$ ) as well as  $W^+Z$  and  $W^-Z$  production. The last two columns contain the relative NLO and NNLO corrections. “Combined” refers to the *sum* of all separate contributions.

Category III differs from Category I only by an additional cut on  $m_{T,W}$ , whose distribution in Category I is shown separately for the SF and DF channels in the left and centre plots of figure 13. For reference we have added a green vertical line at  $m_{T,W} = 120 \text{ GeV}$ , which indicates the additional cut in Category III. Apparently, the  $m_{T,W}$  tail, which is dominated by off-shell  $W$  bosons, is considerably higher in the SF channel than in the DF channel. Thus, the origin of the different SF and DF rates is a different distribution of events, which are moved from the  $W$ -peak region to the tail.

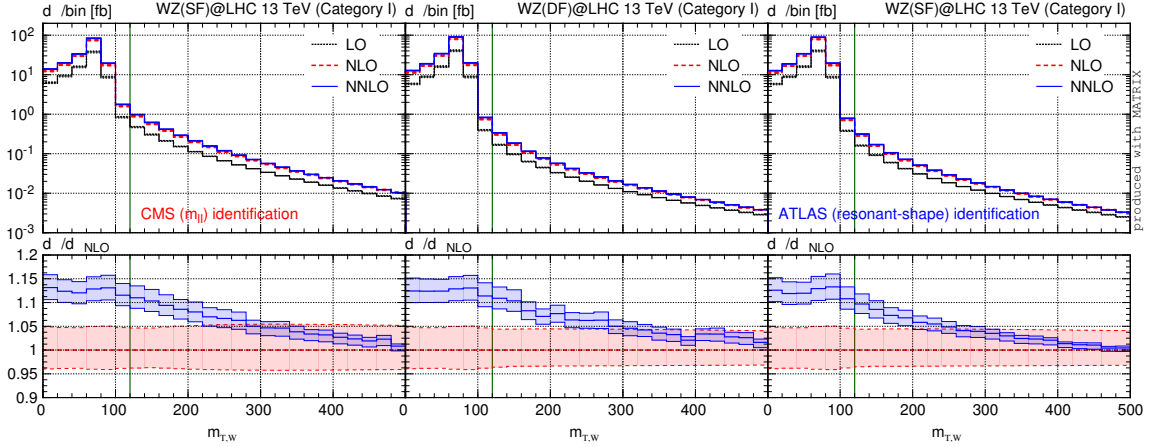


**Figure 13.** Distributions with respect to  $m_{T,W}$  in the fiducial phase space without additional cuts (Category I); left: SF channel; centre: DF channel; right: SF channel, but using the resonant-shape identification of  $W$  and  $Z$  bosons as used by ATLAS. The green vertical line indicates the cut of  $m_{T,W} > 120$  GeV in Category III.

This behaviour is not a particular feature of the SF channel, but a consequence of the  $Z$  (and  $W$ ) identification we are using, which is entirely based on the invariant masses of the two possible combinations of OSSF pairs, by associating the  $Z$  boson with the one closer to the  $Z$  mass. We have repeated the computation of the  $m_{T,W}$  distribution by replacing the CMS identification with the ATLAS resonant-shape identification (see section 3.1 and in particular eq. (3.1)). The ensuing distribution is shown in the right plot of figure 13. Indeed, by eye, no difference between right (SF channel with ATLAS identification) and centre (DF channel) plot is visible. We stress that in the DF channel the  $Z$  and  $W$  bosons are unambiguously identified by the lepton flavours in the final state. The resonant-shape identification takes into account information on both the  $W$ - and the  $Z$ -boson propagators in the dominant double-resonant topologies, which leads to a more accurate modelling of the  $W$ -boson peak in the  $m_{T,W}$  distribution. This identification procedure distributes less events into the tail (similar to the DF channel) than the CMS identification. The resonant-shape identification is therefore much more effective in removing events from the peak region when cutting on  $m_{T,W} > 120$  GeV. This is also reflected by the ensuing total cross sections in Category III: at NNLO, for example, the SF cross section with the resonant-shape identification ( $0.9265(7)^{+1.5\%}_{-1.5\%}$  fb) is of similar size as the one in the DF channel ( $1.010(2)^{+1.6\%}_{-1.6\%}$  fb) as compared to  $3.303(4)^{+1.9\%}_{-1.8\%}$  fb in the SF channel when using the CMS identification. Thus, in more than two out of three events, in Category III the identification of the  $Z$  and the  $W$  boson is swapped in the case of CMS with respect to using the resonant-shape identification. Besides the potential risks that such different identification might have on shapes of certain distributions,<sup>11</sup> a more effective identification

<sup>11</sup>We have checked explicitly several distributions in Category III and found quite substantial differences between SF with CMS identification and DF channels for, e.g.,  $\Delta\phi_{\ell\ell}$ ,  $m_{\ell\ell}$ ,  $m_{\ell\ell\ell}$ ,  $m_{WZ}$ ,  $p_{T,\ell_2}$ ,  $p_{T,\ell_w}$ . These differences are alleviated when using the resonant-shape identification, although some minor differences remain also in that case.

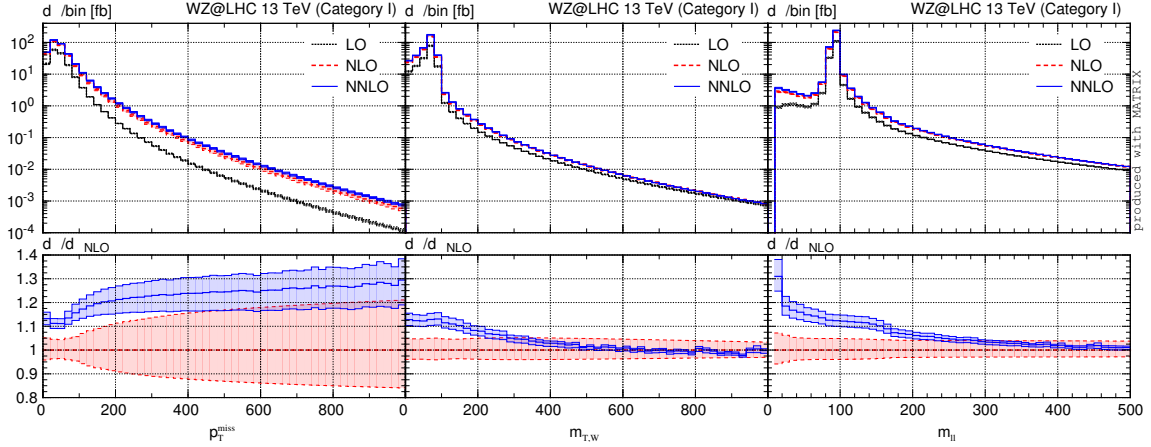


**Figure 14.** Distributions with respect to  $p_T^{\text{miss}}$  (left),  $m_{T,W}$  (centre) and  $m_{\ell\ell}$  (right) in the fiducial phase space without additional cuts (Category I).

would allow to suppress the SM background to new-physics searches in this category by more than a factor of three. Let us finally remark that also Category IV would benefit from a more effective identification, although the effects are much smaller and negative in that case.

In terms of differential distributions, as previously pointed out, the most relevant observables for SUSY searches are  $p_T^{\text{miss}}$ ,  $m_{T,W}$  and  $m_{\ell\ell}$ . These distributions are shown in figure 14 for the first category, i.e. without any additional restrictions on top of the default selection cuts of table 5. The distribution in the missing transverse energy in the left panel of figure 14 features large radiative corrections, ranging up to 30% for the central curve, which, however, primarily affect the normalization. Nevertheless, the shape of the distribution is affected by NNLO corrections at the 10%-20% level in the range up to  $p_T^{\text{miss}} = 1$  TeV. We point out that the rather flat corrections at NNLO can only be achieved by using a dynamic scale (see eq. (3.4)) that takes into account the effects of hard-parton emissions to properly model the tails of the distributions. We have explicitly checked that the NLO  $p_T^{\text{miss}}$  distribution computed with a fixed scale is significantly harder in the tail with relatively large scale uncertainties, while the NNLO cross section — as expected — is quite stable with respect to the scale choice. As a consequence, a fixed scale choice would lead to much larger, but negative NNLO corrections at high transverse momenta. Despite the considerable improvement in the perturbative stability achieved with the use of a dynamic scale, a precise prediction of the fiducial cross section in Categories based on  $p_T^{\text{miss}}$  still requires the inclusion of  $\mathcal{O}(\alpha_S^2)$  terms, since depending on the  $p_T^{\text{miss}}$  cut the NNLO effects may still change by up to 20%.

Similarly, also the  $m_{T,W}$  and  $m_{\ell\ell}$  distributions, in the centre and right plots of figure 14, are subject to sizeable corrections due to the inclusion of  $\mathcal{O}(\alpha_S^2)$  terms. While in the tails of the spectra (for  $m_{T,W} \gtrsim 300$  GeV and  $m_{\ell\ell} \gtrsim 200$  GeV) the NLO and NNLO predictions roughly agree within their respective uncertainties, at smaller  $m_{T,W}$  and  $m_{\ell\ell}$  values the shapes of the distributions are considerably modified, leading to NNLO corrections that

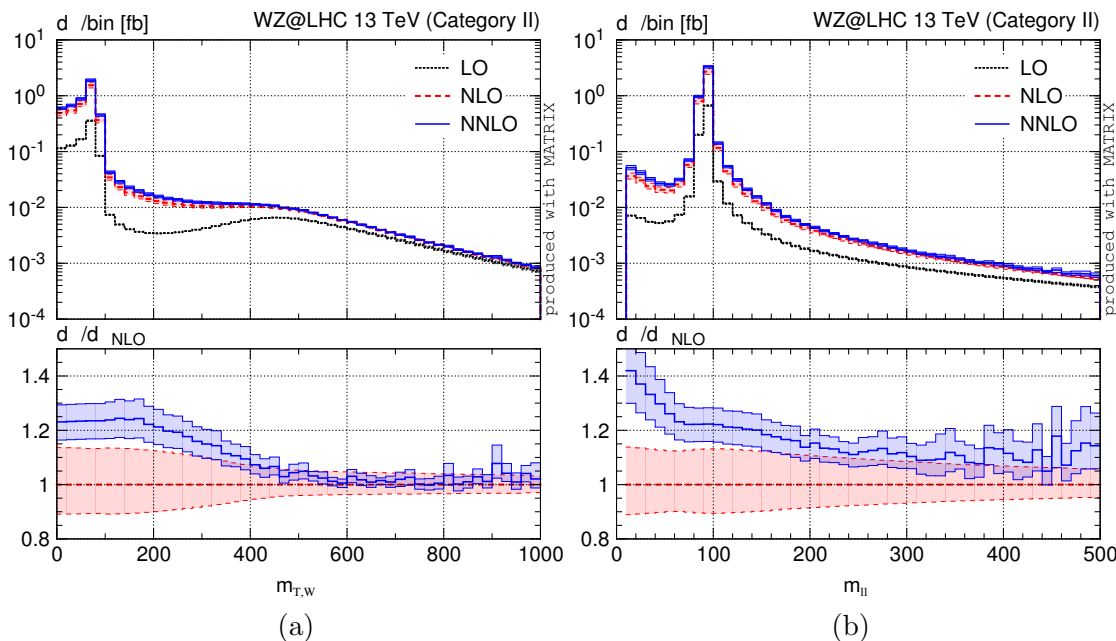


**Figure 15.** Distributions with respect to (a)  $m_{T,W}$  and (b)  $m_{\ell\ell}$  in the fiducial phase space with an additional  $p_T^{\text{miss}} > 200 \text{ GeV}$  cut (Category II).

are not covered by the lower-order uncertainty bands. These differences are alleviated to some extent by the fact that the low- $m_{T,W}$  and  $-m_{\ell\ell}$  regions are usually less important to new-physics searches (where usually the phase-space region below  $m_{T,W} \sim 120 \text{ GeV}$  and  $m_{\ell\ell} \sim 100 \text{ GeV}$ ) is cut), but some region of phase space remains where NNLO corrections ought to be taken into account.

In figure 15 we consider the  $m_{T,W}$  and  $m_{\ell\ell}$  spectra in Category II. Thus, these distributions include an additional cut of  $p_T^{\text{miss}} > 200 \text{ GeV}$  as compared to those in figure 14. As pointed out before, such cut on  $p_T^{\text{miss}}$  requires NNLO accuracy on its own to ensure a proper modelling of the SM background. The specific value of  $200 \text{ GeV}$ , in fact, is incidentally in a region where the NNLO corrections start to become particularly large ( $> 20\%$ ), as can be inferred from the  $p_T^{\text{miss}}$  distribution in figure 14. Indeed, looking at figure 15 both the distribution in  $m_{T,W}$  and  $m_{\ell\ell}$  feature NNLO and NLO cross sections without overlapping uncertainty bands in each peak region, with NNLO corrections of the order of 20%. For small  $m_{\ell\ell}$  values NNLO effects increase up to more than 40%. This region, however, is less relevant to new-physics searches. We note that, when going from NLO to NNLO scale uncertainties are reduced from about 15% to at most 10%. Overall, the results of the two distributions are very similar to the corresponding ones in figure 14 for Category I. Although the NLO and NNLO scale uncertainties are generally larger, the ensuing bands do not overlap around the peak of the distributions.

Figure 16 shows the  $p_T^{\text{miss}}$  and  $m_{\ell\ell}$  spectra while including a cut on  $m_{T,W} > 120 \text{ GeV}$  in addition to the standard selection cuts (Category III). Also in this case the general behaviour of these distributions is quite similar to those in Category I, however, the absolute size of the corrections at NNLO is reduced. Thanks to the dynamic scale choice, the dependence of the NNLO correction on the value of  $p_T^{\text{miss}}$  is quite flat. With a fixed scale

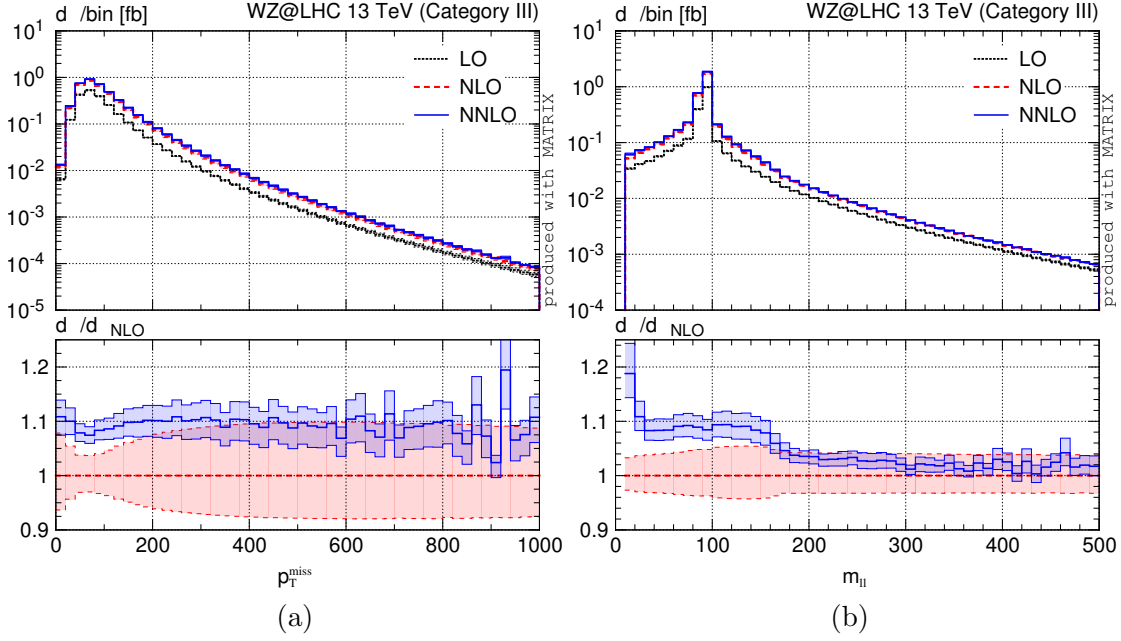


**Figure 16.** Distributions with respect to (a)  $p_T^{\text{miss}}$  and (b)  $m_{\ell\ell}$  in the fiducial phase space with an additional  $m_{T,W} > 120$  GeV cut (Category III).

we find a similarly strong  $p_T^{\text{miss}}$  dependence in the tail of the distribution as pointed out for Category I. NLO and NNLO uncertainty bands feature a satisfactory overlap starting from  $p_T^{\text{miss}} \gtrsim 200$  GeV. The  $m_{\ell\ell}$  distribution shows consistent NLO and NNLO predictions in the tail of the distribution. The NNLO corrections become larger ( $\sim 10\%$ ) only at  $m_{\ell\ell} \lesssim 150$  GeV, where  $W^\pm Z$  production becomes less important as a SM background to new-physics searches. We point out that, as shown in figure 17, the increase of the NNLO corrections at  $m_{\ell\ell} \lesssim 150$  GeV is only present in the SF channel, while the DF channel features a step increase at  $m_{\ell\ell} \lesssim 50$  GeV. It is clear from the main frame of that figure that the distributions in the two channels are modelled very differently, which can again be traced back to the used identification procedure.

In figure 18 the  $p_T^{\text{miss}}$  and  $m_{T,W}$  distributions in Category IV are shown. We see that the  $m_{\ell\ell} > 105$  GeV cut has almost no impact on the shapes of the  $p_T^{\text{miss}}$  and  $m_{T,W}$  spectra, apart from the general reduction of the absolute size of the NNLO corrections compared to Category I. Also in this category NNLO corrections are quantitatively relevant, and their impact on the tails of the distributions is reduced with the use of a dynamic scale.

In conclusion, for the three observables relevant to new-physics searches that have been considered in this section, the sizeable (10%-30%) NNLO corrections depend on the specific cut values. This demands NNLO accurate predictions for the  $W^\pm Z$  background when categories based on these observables are defined. Furthermore, a dynamic scale choice is crucial to properly model the various distributions, in particular the tail of the  $p_T^{\text{miss}}$  spectrum. Moreover, NNLO corrections considerably reduce the perturbative uncertainties in all three distributions we investigated, regardless of the category under consideration.



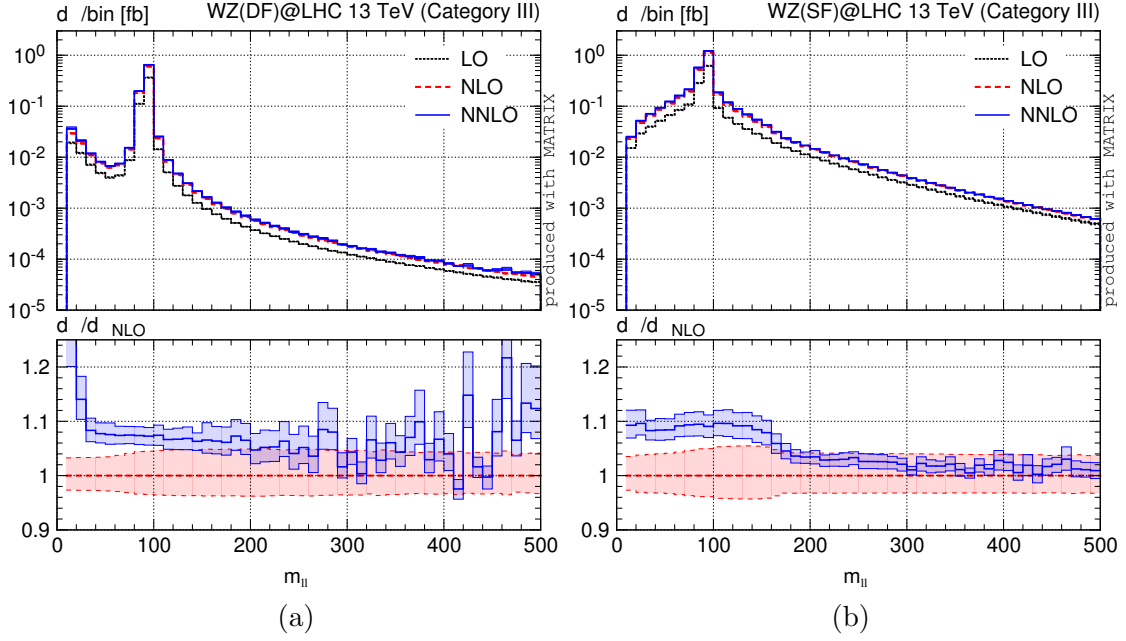


**Figure 17.** Distributions with respect to  $m_{\ell\ell}$  in the fiducial phase space with an additional  $m_{T,W} > 120$  GeV cut (Category III), for (a) the SF and (b) the DF channel.

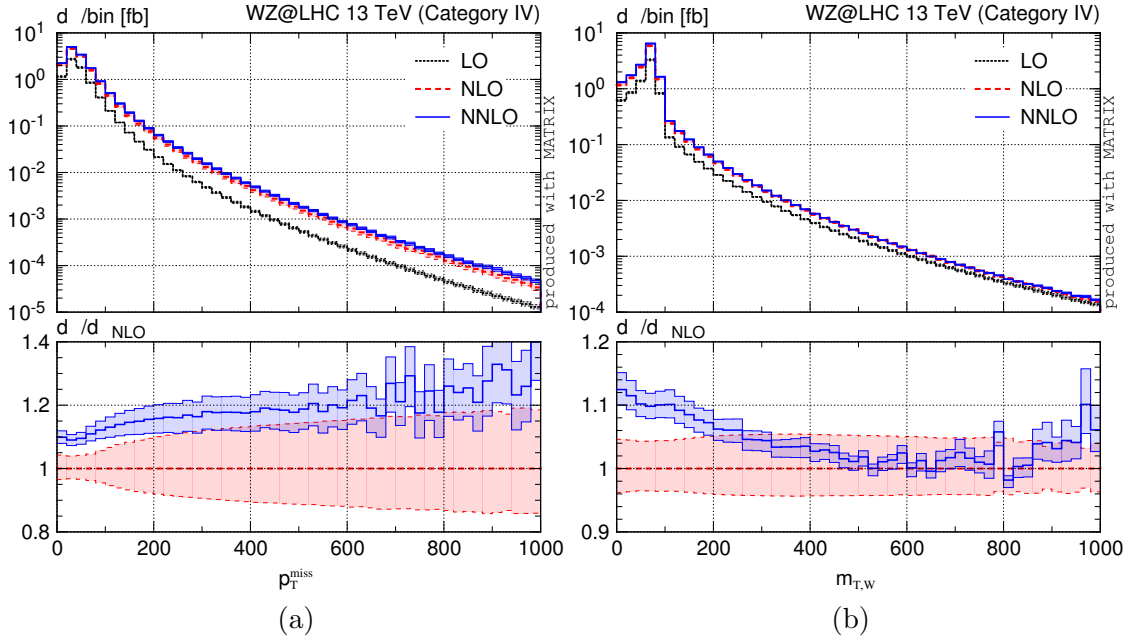


**Figure 18.** Distributions with respect to (a)  $p_T^{\text{miss}}$  and (b)  $m_{T,W}$  in the fiducial phase space with an additional  $m_{\ell\ell} > 105$  GeV cut (Category IV).

## 4 Summary

In this paper, we have presented the first computation of fully differential cross sections for the production of a  $W^\pm Z$  pair at NNLO in QCD perturbation theory. Our computation consistently includes the leptonic decays of the weak bosons accounting for off-shell effects,



spin correlations and interference contributions in all double-, single- and non-resonant configurations in the complex-mass scheme, i.e. we have performed a complete calculation for the process  $pp \rightarrow \ell'^{\pm} \nu_{\ell'} \ell^{-} \ell^{+} + X$  with  $\ell, \ell' \in \{e, \mu\}$ , both in the SF and in the DF channel. Our results are obtained with the numerical program MATRIX, which employs the  $q_T$ -subtraction method to evaluate NNLO QCD corrections to a wide class of processes. We have shown that the ensuing fiducial cross sections and distributions depend very mildly on the technical cut-off parameter  $r_{\text{cut}}$ , thereby allowing us to numerically control the predicted NNLO cross section at the one-permille level or better.

We have presented a comprehensive comparison of our numerical predictions with the available data from ATLAS and CMS at  $\sqrt{s} = 8$  and 13 TeV for both the fiducial cross sections and differential distributions in  $W^{\pm}Z$  production. As in the case of the inclusive cross section [18] QCD radiative corrections are essential to properly model the  $W^{\pm}Z$  cross section. They amount to up to 85% at NLO, and NNLO corrections further increase the NLO result by about 10%. The inclusion of NNLO corrections significantly improves the agreement with the measured cross sections by ATLAS at both 8 and 13 TeV centre-of-mass energies. The 13 TeV CMS result is somewhat ( $\sim 2.6\sigma$ ) lower than the theoretical prediction, which is about the same discrepancy that has been observed in the result extrapolated to the total inclusive cross section [18]. The full data set collected by the end of 2016 ( $\sim 40 \text{ fb}^{-1}$ ) will show whether this difference is a plain statistical effect of the small data set ( $\sim 2.3 \text{ fb}^{-1}$ ) used for that measurement.

Distributions in the fiducial phase space of the  $\ell\ell\nu$  final states are available only for the ATLAS 8 TeV data set. Our comparison reveals a remarkable agreement with the measured cross section in each bin upon inclusion of higher-order corrections, being typically within  $1\sigma$  of the quoted experimental errors. Although this statement holds already at NLO, the NNLO cross sections display an improved description of the data not only in terms of normalization, but also regarding the shapes. Only the distribution in the missing transverse energy exhibits some tension between theory and data: we observe deviations at the level of  $1\sigma - 2\sigma$  in some bins, leading to a more evident discrepancy in the shape of the distribution. We have shown that this discrepancy is present only in  $W^{-}Z$  production, while our NNLO prediction nicely describes the data in the case of  $W^{+}Z$  production.

We have further shown that our computation of the ratio of  $W^{+}Z$  over  $W^{-}Z$  distributions agrees well with the experimental data, given the rather large experimental uncertainties. Along with this study we have pointed out a number of distributions which signal significant differences between  $W^{+}Z$  and  $W^{-}Z$  production, and may be sensitive to disentangle genuine perturbative effects at NNLO.

We have completed our phenomenological study by considering a scenario where  $W^{\pm}Z$  production is a background to new-physics searches in the three leptons plus missing energy channel. NNLO effects on the background rates have been discussed in the relevant categories, together with the corresponding distributions. Our findings can be summarized as follows:

- LO predictions cannot be used to model cross sections and distributions in a meaningful way: the size of NLO corrections can be, in some categories, of the order of several hundred percent.

- NNLO corrections on the  $W^\pm Z$  rates range between roughly 8% and 23%, while distributions are subject to considerable shape distortions when going from NLO to NNLO.
- For cuts on the  $p_T^{\text{miss}}$  observable, which is particularly important for categorization in new-physics scenarios, NNLO corrections turn out to be particularly important, as they may vary between 10%-30% depending on the specific value of the cut.
- Only using a dynamic scale (see eq. (3.4)) the shape of the relevant distributions is perturbatively stable. This is in particular true for the  $p_T^{\text{miss}}$  distribution, which was found to be drastically impacted by NNLO corrections if a fixed scale was applied.
- Finally, we have shown that in the SF channel an identification of the  $Z$  boson based solely on how close the dilepton-pair mass is to  $m_Z$  may lead to some problems: when a  $m_{T,W} > 120 \text{ GeV}$  cut is enforced, in more than two out of three events the  $Z$ - and  $W$ -boson identification is swapped, leading to a difference in the SF and DF rates by more than a factor of three. We find that a resonant-shape identification (see eq. (3.1)) is much more efficient, thereby leading to a more effective background suppression.

We conclude by adding a few comments about the residual uncertainties of our calculation. As is customary in perturbative QCD computations, the uncertainties from missing higher-order contributions were estimated by studying scale variations. We have seen that, when going from NLO to NNLO scale uncertainties are generally reduced both for fiducial cross sections and for kinematical distributions. It should be noted, however, that the uncertainties seem to underestimate the size of missing higher-order corrections at LO and NLO. This tendency decreases with increasing perturbative order: while the LO uncertainty grossly underestimates the size of the NLO corrections (which, for this process, is in part due to the existence of an approximate radiation zero), the NLO and NNLO predictions are much closer, and almost consistent within uncertainties. Considering that at NNLO all partonic channels are included and no regions of phase space that are effectively only LO-accurate remain, we conclude that the  $\mathcal{O}(2 - 5\%)$  NNLO uncertainties on our fiducial cross sections (see tables 2, 3, 4 and 6) are expected to provide the correct order of magnitude of yet uncalculated higher-order contributions. EW corrections would affect the fiducial cross sections at the 1% level or less [16, 17], but are expected to become relevant in the tails of the distributions, which will be potentially important for new-physics searches. The inclusion of EW corrections is, however, left to future investigations. PDF uncertainties are expected to be at the 1%–2% level.

We believe that the calculation and the results presented in this paper will be highly valuable both for experimental measurements of the  $W^\pm Z$  signal and in new-physics searches involving the three lepton plus missing energy signature. The computation is available in the numerical program MATRIX, which is able to carry out fully-exclusive NNLO computations for a wide class of processes at hadron colliders. We plan to release a public version of our program in the near future.

channel	$\sigma_{\text{LO}}$ [fb]	$\sigma_{\text{NLO}}$ [fb]	$\sigma_{\text{NNLO}}$ [fb]	$\sigma_{\text{CMS}}$ [fb]
$\mu^+e^+e^-$	$14.72(0)^{+2.1\%}_{-2.9\%}$	$26.05(1)^{+5.4\%}_{-4.1\%}$	$28.16(1)^{+1.8\%}_{-1.9\%}$	
$e^+\mu^+\mu^-$				
$e^+e^+e^-$	$15.14(0)^{+2.1\%}_{-3.0\%}$	$26.97(1)^{+5.5\%}_{-4.2\%}$	$29.20(2)^{+1.8\%}_{-1.9\%}$	
$\mu^+\mu^+\mu^-$				
combined	$59.72(1)^{+2.1\%}_{-3.0\%}$	$106.0(0)^{+5.5\%}_{-4.1\%}$	$114.7(1)^{+1.8\%}_{-1.9\%}$	
$\mu^-e^+e^-$	$8.432(1)^{+2.4\%}_{-3.3\%}$	$15.62(0)^{+5.9\%}_{-4.5\%}$	$16.98(1)^{+1.9\%}_{-2.0\%}$	
$e^-\mu^+\mu^-$				
$e^-e^+e^-$	$8.710(1)^{+2.4\%}_{-3.4\%}$	$16.24(0)^{+5.9\%}_{-4.5\%}$	$17.72(1)^{+1.9\%}_{-2.0\%}$	
$\mu^-\mu^+\mu^-$				
combined	$34.28(0)^{+2.4\%}_{-3.3\%}$	$63.72(2)^{+5.9\%}_{-4.5\%}$	$69.39(4)^{+1.9\%}_{-2.0\%}$	
$\mu^\pm e^+e^-$	$23.15(0)^{+2.2\%}_{-3.1\%}$	$41.67(1)^{+5.6\%}_{-4.3\%}$	$45.13(2)^{+1.8\%}_{-1.9\%}$	
$e^\pm\mu^+\mu^-$				
$e^\pm e^+e^-$	$23.86(0)^{+2.2\%}_{-3.1\%}$	$43.21(1)^{+5.6\%}_{-4.3\%}$	$46.91(3)^{+1.9\%}_{-2.0\%}$	
$\mu^\pm\mu^+\mu^-$				
combined	$94.01(1)^{+2.2\%}_{-3.1\%}$	$169.8(0)^{+5.6\%}_{-4.3\%}$	$184.1(1)^{+1.8\%}_{-1.9\%}$	

**Table 7.** Fiducial cross sections for CMS 8 TeV. Note that due to the flavour-unspecific lepton cuts the theoretical predictions are flavour-blind, which is why the results are symmetric under  $e \leftrightarrow \mu$  exchange. No CMS data for the fiducial cross sections available at 8 TeV. “Combined” refers to the *sum* of all separate contributions.

## Acknowledgments

We would like to thank Lucia Di Ciaccio, Günther Dissertori, Thomas Gehrmann, Constantin Heidegger, Jan Hoss and Kenneth Long for useful discussions and comments on the manuscript. This research was supported in part by the Swiss National Science Foundation (SNF) under contracts CRSII2-141847, 200020-169041, by the Research Executive Agency (REA) of the European Union under the Grant Agreement number PITN-GA-2012-316704 (*HiggsTools*), and by the National Science Foundation under Grant No. NSF PHY11-25915. MW has been partially supported by ERC Consolidator Grant 614577 HICCUP.

## A CMS cross sections at 8 TeV and 13 TeV

For completeness we quote below the cross-section predictions in the fiducial phase space for CMS at 8 TeV and 13 TeV, separated by the individual leptonic channels in table 7 and table 8, respectively.

channel	$\sigma_{\text{LO}}$ [fb]	$\sigma_{\text{NLO}}$ [fb]	$\sigma_{\text{NNLO}}$ [fb]	$\sigma_{\text{CMS}}$ [fb]
$\mu^+e^+e^-$	$22.08(0)^{+5.2\%}_{-6.2\%}$	$43.91(1)^{+5.4\%}_{-4.3\%}$	$48.53(2)^{+2.2\%}_{-2.0\%}$	
$e^+\mu^+\mu^-$				
$e^+e^+e^-$	$22.73(0)^{+5.2\%}_{-6.2\%}$	$45.48(1)^{+5.4\%}_{-4.4\%}$	$50.39(3)^{+2.3\%}_{-2.1\%}$	
$\mu^+\mu^+\mu^-$				
combined	$89.62(1)^{+5.2\%}_{-6.2\%}$	$178.8(0)^{+5.4\%}_{-4.3\%}$	$197.8(1)^{+2.3\%}_{-2.1\%}$	
$\mu^-e^+e^-$	$14.45(0)^{+5.6\%}_{-6.7\%}$	$30.04(1)^{+5.6\%}_{-4.5\%}$	$33.40(2)^{+2.4\%}_{-2.1\%}$	
$e^-\mu^+\mu^-$				
$e^-e^+e^-$	$14.92(0)^{+5.6\%}_{-6.7\%}$	$31.25(1)^{+5.7\%}_{-4.6\%}$	$34.83(2)^{+2.4\%}_{-2.2\%}$	
$\mu^-\mu^+\mu^-$				
combined	$58.72(1)^{+5.6\%}_{-6.7\%}$	$122.6(0)^{+5.7\%}_{-4.6\%}$	$136.5(1)^{+2.4\%}_{-2.2\%}$	
$\mu^\pm e^+e^-$	$36.52(0)^{+5.3\%}_{-6.4\%}$	$73.95(2)^{+5.5\%}_{-4.4\%}$	$81.93(4)^{+2.3\%}_{-2.1\%}$	
$e^\pm\mu^+\mu^-$				
$e^\pm e^+e^-$	$37.65(0)^{+5.4\%}_{-6.4\%}$	$76.74(2)^{+5.5\%}_{-4.4\%}$	$85.22(5)^{+2.3\%}_{-2.1\%}$	
$\mu^\pm\mu^+\mu^-$				
combined	$148.3(0)^{+5.4\%}_{-6.4\%}$	$301.4(1)^{+5.5\%}_{-4.4\%}$	$334.3(2)^{+2.3\%}_{-2.1\%}$	$258 \pm 8.1\%(\text{stat})^{+7.4\%}_{-7.7\%}(\text{syst}) \pm 3.1(\text{lumi})$

**Table 8.** Fiducial cross sections for CMS 13 TeV. Note that due to the flavour-unspecific lepton cuts the theoretical predictions are flavour-blind, which is why the results are symmetric under  $e \leftrightarrow \mu$  exchange. The available CMS data from refs. [8] are also shown. “Combined” refers to the *sum* of all separate contributions.

**Open Access.** This article is distributed under the terms of the Creative Commons Attribution License ([CC-BY 4.0](https://creativecommons.org/licenses/by/4.0/)), which permits any use, distribution and reproduction in any medium, provided the original author(s) and source are credited.

## References

- [1] D.E. Morrissey, T. Plehn and T.M.P. Tait, *Physics searches at the LHC*, *Phys. Rept.* **515** (2012) 1 [[arXiv:0912.3259](https://arxiv.org/abs/0912.3259)] [[INSPIRE](#)].
- [2] CDF collaboration, T. Aaltonen et al., *Measurement of the WZ Cross section and Triple Gauge Couplings in  $p\bar{p}$  Collisions at  $\sqrt{s} = 1.96$  TeV*, *Phys. Rev. D* **86** (2012) 031104 [[arXiv:1202.6629](https://arxiv.org/abs/1202.6629)] [[INSPIRE](#)].
- [3] D0 collaboration, V.M. Abazov et al., *A measurement of the WZ and ZZ production cross sections using leptonic final states in  $8.6 \text{ fb}^{-1}$  of  $p\bar{p}$  collisions*, *Phys. Rev. D* **85** (2012) 112005 [[arXiv:1201.5652](https://arxiv.org/abs/1201.5652)] [[INSPIRE](#)].
- [4] ATLAS collaboration, *Measurement of WZ production in proton-proton collisions at  $\sqrt{s} = 7$  TeV with the ATLAS detector*, *Eur. Phys. J. C* **72** (2012) 2173 [[arXiv:1208.1390](https://arxiv.org/abs/1208.1390)] [[INSPIRE](#)].

- [5] CMS collaboration, *Measurement of the WZ production cross section in pp collisions at  $\sqrt{s} = 7$  and 8 TeV and search for anomalous triple gauge couplings at  $\sqrt{s} = 8$  TeV*, *Eur. Phys. J. C* **77** (2017) 236 [[arXiv:1609.05721](#)] [[INSPIRE](#)].
- [6] ATLAS collaboration, *Measurements of  $W^{\pm}Z$  production cross sections in pp collisions at  $\sqrt{s} = 8$  TeV with the ATLAS detector and limits on anomalous gauge boson self-couplings*, *Phys. Rev. D* **93** (2016) 092004 [[arXiv:1603.02151](#)] [[INSPIRE](#)].
- [7] ATLAS collaboration, *Measurement of the  $W^{\pm}Z$  boson pair-production cross section in pp collisions at  $\sqrt{s} = 13$  TeV with the ATLAS Detector*, *Phys. Lett. B* **762** (2016) 1 [[arXiv:1606.04017](#)] [[INSPIRE](#)].
- [8] CMS collaboration, *Measurement of the WZ production cross section in pp collisions at  $\sqrt{s} = 13$  TeV*, *Phys. Lett. B* **766** (2017) 268 [[arXiv:1607.06943](#)] [[INSPIRE](#)].
- [9] J. Ohnemus, *An Order  $\alpha^{-s}$  calculation of hadronic  $W^{\pm}Z$  production*, *Phys. Rev. D* **44** (1991) 3477.
- [10] J. Ohnemus, *Hadronic ZZ,  $W^{-}W^{+}$  and  $W^{\pm}Z$  production with QCD corrections and leptonic decays*, *Phys. Rev. D* **50** (1994) 1931 [[hep-ph/9403331](#)] [[INSPIRE](#)].
- [11] J.M. Campbell and R.K. Ellis, *An Update on vector boson pair production at hadron colliders*, *Phys. Rev. D* **60** (1999) 113006 [[hep-ph/9905386](#)] [[INSPIRE](#)].
- [12] L.J. Dixon, Z. Kunszt and A. Signer, *Vector boson pair production in hadronic collisions at order  $\alpha_s$ : Lepton correlations and anomalous couplings*, *Phys. Rev. D* **60** (1999) 114037 [[hep-ph/9907305](#)] [[INSPIRE](#)].
- [13] J.M. Campbell, R.K. Ellis and C. Williams, *Vector boson pair production at the LHC*, *JHEP* **07** (2011) 018 [[arXiv:1105.0020](#)] [[INSPIRE](#)].
- [14] L.J. Dixon, Z. Kunszt and A. Signer, *Helicity amplitudes for  $O(\alpha_s)$  production of  $W^{+}W^{-}$ ,  $W^{\pm}Z$ ,  $ZZ$ ,  $W^{\pm}\gamma$ , or  $Z\gamma$  pairs at hadron colliders*, *Nucl. Phys. B* **531** (1998) 3 [[hep-ph/9803250](#)] [[INSPIRE](#)].
- [15] F. Campanario, C. Englert, S. Kallweit, M. Spannowsky and D. Zeppenfeld, *NLO QCD corrections to WZ+jet production with leptonic decays*, *JHEP* **07** (2010) 076 [[arXiv:1006.0390](#)] [[INSPIRE](#)].
- [16] A. Bierweiler, T. Kasprzik and J.H. Kühn, *Vector-boson pair production at the LHC to  $O(\alpha^3)$  accuracy*, *JHEP* **12** (2013) 071 [[arXiv:1305.5402](#)] [[INSPIRE](#)].
- [17] J. Baglio, L.D. Ninh and M.M. Weber, *Massive gauge boson pair production at the LHC: a next-to-leading order story*, *Phys. Rev. D* **88** (2013) 113005 [[arXiv:1307.4331](#)] [[INSPIRE](#)].
- [18] M. Grazzini, S. Kallweit, D. Rathlev and M. Wiesemann,  *$W^{\pm}Z$  production at hadron colliders in NNLO QCD*, *Phys. Lett. B* **761** (2016) 179 [[arXiv:1604.08576](#)] [[INSPIRE](#)].
- [19] T. Gehrmann, A. von Manteuffel and L. Tancredi, *The two-loop helicity amplitudes for  $q\bar{q}' \rightarrow V_1 V_2 \rightarrow 4$  leptons*, *JHEP* **09** (2015) 128 [[arXiv:1503.04812](#)] [[INSPIRE](#)].
- [20] F. Caola, J.M. Henn, K. Melnikov, A.V. Smirnov and V.A. Smirnov, *Two-loop helicity amplitudes for the production of two off-shell electroweak bosons in quark-antiquark collisions*, *JHEP* **11** (2014) 041 [[arXiv:1408.6409](#)] [[INSPIRE](#)].
- [21] A. Denner, S. Dittmaier, M. Roth and L.H. Wieders, *Electroweak corrections to charged-current  $e^{+}e^{-} \rightarrow 4$  fermion processes: Technical details and further results*, *Nucl. Phys. B* **724** (2005) 247 [Erratum *ibid.* **B 854** (2012) 504] [[hep-ph/0505042](#)] [[INSPIRE](#)].

- [22] S. Catani and M. Grazzini, *An NNLO subtraction formalism in hadron collisions and its application to Higgs boson production at the LHC*, *Phys. Rev. Lett.* **98** (2007) 222002 [[hep-ph/0703012](#)] [[INSPIRE](#)].
- [23] G. Bozzi, S. Catani, D. de Florian and M. Grazzini, *Transverse-momentum resummation and the spectrum of the Higgs boson at the LHC*, *Nucl. Phys. B* **737** (2006) 73 [[hep-ph/0508068](#)] [[INSPIRE](#)].
- [24] S. Catani and M.H. Seymour, *The Dipole formalism for the calculation of QCD jet cross-sections at next-to-leading order*, *Phys. Lett. B* **378** (1996) 287 [[hep-ph/9602277](#)] [[INSPIRE](#)].
- [25] S. Catani and M.H. Seymour, *A General algorithm for calculating jet cross-sections in NLO QCD*, *Nucl. Phys. B* **485** (1997) 291 [Erratum *ibid.* **B 510** (1998) 503] [[hep-ph/9605323](#)] [[INSPIRE](#)].
- [26] F. Cascioli, P. Maierhöfer and S. Pozzorini, *Scattering Amplitudes with Open Loops*, *Phys. Rev. Lett.* **108** (2012) 111601 [[arXiv:1111.5206](#)] [[INSPIRE](#)].
- [27] A. Denner, S. Dittmaier and L. Hofer, *COLLIER — A fortran-library for one-loop integrals*, *PoS(LL2014)071* [[arXiv:1407.0087](#)] [[INSPIRE](#)].
- [28] A. Denner, S. Dittmaier and L. Hofer, *Collier: a fortran-based Complex One-Loop Library in Extended Regularizations*, *Comput. Phys. Commun.* **212** (2017) 220 [[arXiv:1604.06792](#)] [[INSPIRE](#)].
- [29] M. Grazzini, S. Kallweit, D. Rathlev and M. Wiesemann, *Transverse-momentum resummation for vector-boson pair production at NNLL+NNLO*, *JHEP* **08** (2015) 154 [[arXiv:1507.02565](#)] [[INSPIRE](#)].
- [30] M. Wiesemann, *Transverse-momentum resummation of colorless final states at the NNLL+NNLO*, *PoS(RADCOR2015)026* [[arXiv:1602.03401](#)] [[INSPIRE](#)].
- [31] S. Catani, L. Cieri, D. de Florian, G. Ferrera and M. Grazzini, *Universality of transverse-momentum resummation and hard factors at the NNLO*, *Nucl. Phys. B* **881** (2014) 414 [[arXiv:1311.1654](#)] [[INSPIRE](#)].
- [32] S. Catani, L. Cieri, D. de Florian, G. Ferrera and M. Grazzini, *Vector boson production at hadron colliders: hard-collinear coefficients at the NNLO*, *Eur. Phys. J. C* **72** (2012) 2195 [[arXiv:1209.0158](#)] [[INSPIRE](#)].
- [33] T. Gehrmann, T. Lübbert and L.L. Yang, *Transverse parton distribution functions at next-to-next-to-leading order: the quark-to-quark case*, *Phys. Rev. Lett.* **109** (2012) 242003 [[arXiv:1209.0682](#)] [[INSPIRE](#)].
- [34] T. Gehrmann, T. Lübbert and L.L. Yang, *Calculation of the transverse parton distribution functions at next-to-next-to-leading order*, *JHEP* **06** (2014) 155 [[arXiv:1403.6451](#)] [[INSPIRE](#)].
- [35] T. Matsuura, S.C. van der Marck and W. van Neerven, *The Calculation of the Second Order Soft and Virtual Contributions to the Drell-Yan Cross-Section*, *Nucl. Phys. B* **319** (1989) 570.
- [36] T. Gehrmann and L. Tancredi, *Two-loop QCD helicity amplitudes for  $q\bar{q} \rightarrow W^\pm \gamma$  and  $q\bar{q} \rightarrow Z^0 \gamma$* , *JHEP* **02** (2012) 004 [[arXiv:1112.1531](#)] [[INSPIRE](#)].
- [37] M. Grazzini, S. Kallweit, D. Rathlev and A. Torre,  *$Z\gamma$  production at hadron colliders in NNLO QCD*, *Phys. Lett. B* **731** (2014) 204 [[arXiv:1309.7000](#)] [[INSPIRE](#)].



- [38] M. Grazzini, S. Kallweit and D. Rathlev,  $W\gamma$  and  $Z\gamma$  production at the LHC in NNLO QCD, *JHEP* **07** (2015) 085 [[arXiv:1504.01330](#)] [[INSPIRE](#)].
- [39] F. Cascioli et al., ZZ production at hadron colliders in NNLO QCD, *Phys. Lett. B* **735** (2014) 311 [[arXiv:1405.2219](#)] [[INSPIRE](#)].
- [40] M. Grazzini, S. Kallweit and D. Rathlev, ZZ production at the LHC: fiducial cross sections and distributions in NNLO QCD, *Phys. Lett. B* **750** (2015) 407 [[arXiv:1507.06257](#)] [[INSPIRE](#)].
- [41] T. Gehrmann et al.,  $W^+W^-$  Production at Hadron Colliders in Next to Next to Leading Order QCD, *Phys. Rev. Lett.* **113** (2014) 212001 [[arXiv:1408.5243](#)] [[INSPIRE](#)].
- [42] M. Grazzini, S. Kallweit, S. Pozzorini, D. Rathlev and M. Wiesemann,  $W^+W^-$  production at the LHC: fiducial cross sections and distributions in NNLO QCD, *JHEP* **08** (2016) 140 [[arXiv:1605.02716](#)] [[INSPIRE](#)].
- [43] U. Baur, T. Han and J. Ohnemus, Amplitude zeros in  $W^\pm Z$  production, *Phys. Rev. Lett.* **72** (1994) 3941 [[hep-ph/9403248](#)] [[INSPIRE](#)].
- [44] CMS collaboration, Search for electroweak SUSY production in multilepton final states in pp collisions at  $\sqrt{s} = 13$  TeV with 12.9/fb, *CMS-PAS-SUS-16-024* (2016).
- [45] F. Cascioli, J. Lindert, P. Maierhöfer and S. Pozzorini, The OPENLOOPS one-loop generator, is publicly available at <http://openloops.hepforge.org>.
- [46] A. Denner, S. Dittmaier and L. Hofer, COLLIER — A Complex One-Loop LLibrary with Extended Regularizations, is publicly available at <http://collier.hepforge.org>.
- [47] A. Denner and S. Dittmaier, Reduction of one loop tensor five point integrals, *Nucl. Phys. B* **658** (2003) 175 [[hep-ph/0212259](#)] [[INSPIRE](#)].
- [48] A. Denner and S. Dittmaier, Reduction schemes for one-loop tensor integrals, *Nucl. Phys. B* **734** (2006) 62 [[hep-ph/0509141](#)] [[INSPIRE](#)].
- [49] A. Denner and S. Dittmaier, Scalar one-loop 4-point integrals, *Nucl. Phys. B* **844** (2011) 199 [[arXiv:1005.2076](#)] [[INSPIRE](#)].
- [50] G. Ossola, C.G. Papadopoulos and R. Pittau, CutTools: A Program implementing the OPP reduction method to compute one-loop amplitudes, *JHEP* **03** (2008) 042 [[arXiv:0711.3596](#)] [[INSPIRE](#)].
- [51] A. van Hameren, OneLOop: For the evaluation of one-loop scalar functions, *Comput. Phys. Commun.* **182** (2011) 2427 [[arXiv:1007.4716](#)] [[INSPIRE](#)].
- [52] T. Gehrmann, A. von Manteuffel and L. Tancredi, The VVAMP project, is publicly available at <http://vvamp.hepforge.org>.
- [53] J. Vollinga and S. Weinzierl, Numerical evaluation of multiple polylogarithms, *Comput. Phys. Commun.* **167** (2005) 177 [[hep-ph/0410259](#)] [[INSPIRE](#)].
- [54] C.W. Bauer, A. Frink and R. Kreckel, Introduction to the GiNaC framework for symbolic computation within the C++ programming language, *J. Symb. Comput.* **33** (2000) 1.
- [55] S. Catani, S. Dittmaier, M.H. Seymour and Z. Trócsányi, The Dipole formalism for next-to-leading order QCD calculations with massive partons, *Nucl. Phys. B* **627** (2002) 189 [[hep-ph/0201036](#)] [[INSPIRE](#)].



- [56] S. Kallweit, J.M. Lindert, P. Maierhöfer, S. Pozzorini and M. Schönherr, *NLO electroweak automation and precise predictions for  $W$ +multijet production at the LHC*, *JHEP* **04** (2015) 012 [[arXiv:1412.5157](#)] [[INSPIRE](#)].
- [57] S. Kallweit, J.M. Lindert, P. Maierhöfer, S. Pozzorini and M. Schönherr, *NLO QCD+EW predictions for  $V$  + jets including off-shell vector-boson decays and multijet merging*, *JHEP* **04** (2016) 021 [[arXiv:1511.08692](#)] [[INSPIRE](#)].
- [58] D. de Florian and M. Grazzini, *The Structure of large logarithmic corrections at small transverse momentum in hadronic collisions*, *Nucl. Phys. B* **616** (2001) 247 [[hep-ph/0108273](#)] [[INSPIRE](#)].
- [59] S. Catani and M. Grazzini, *Higgs Boson Production at Hadron Colliders: Hard-Collinear Coefficients at the NNLO*, *Eur. Phys. J. C* **72** (2012) 2013 [Erratum *ibid.* **C 72** (2012) 2132] [[arXiv:1106.4652](#)] [[INSPIRE](#)].
- [60] PARTICLE DATA GROUP collaboration, K.A. Olive et al., *Review of Particle Physics*, *Chin. Phys. C* **38** (2014) 090001
- [61] NNPDF collaboration, R.D. Ball et al., *Parton distributions for the LHC Run II*, *JHEP* **04** (2015) 040 [[arXiv:1410.8849](#)] [[INSPIRE](#)].
- [62] M. Cacciari, G.P. Salam and G. Soyez, *The Anti- $k(t)$  jet clustering algorithm*, *JHEP* **04** (2008) 063 [[arXiv:0802.1189](#)] [[INSPIRE](#)].
- [63] F. Campanario, M. Kerner, L.D. Ninh and D. Zeppenfeld, *WZ Production in Association with Two Jets at Next-to-Leading Order in QCD*, *Phys. Rev. Lett.* **111** (2013) 052003 [[arXiv:1305.1623](#)] [[INSPIRE](#)].